Dissertation

submitted to the

Combined Faculties for the
Natural Sciences and for Mathematics
of the Ruperto-Carola University of Heidelberg,
Germany
for the degree of

Doctor of Natural Sciences

Put forward by
Dipl. Phys. Matthias Benjamin Henrich
Born in Herrenberg

date of oral examination
May 14th 2014

In der Hoffnung, dass diese Arbeit tatsächlich
der Krebsforschung dienen kann.

gewidmet

Markus Henrich (1948-2004)

The Potential of Semiconductor Lasers for STED Nanoscopy

Referees:

Prof. Dr. Stefan W. Hell
Prof. Dr. Wolfgang Petrich

Abstract

Twenty years after it was proposed, STED nanoscopy has evolved into a powerful tool in far-field fluorescence imaging which achieves resolutions below $20nm$. Nevertheless, the application of STED nanoscopy in life sciences on a large scale is hindered by the high effort which the method requires. This effort is in great part due to the STED laser. So far, lasers which can be utilized for STED, e.g. titanium-sapphire lasers, show both, technical and practical shortcomings, resulting in complex nanoscopy systems.
Semiconductor lasers which are compact, reliable and controllable without effort, are predestinated to improve this situation if they are adapted to meet the pulse requirements for STED. Therefore, this thesis examines the potential of different types of semiconductor lasers for STED. Fabry-Pérot laser diodes in overdriven gain switched operation are demonstrated to be suitable STED lasers. Even more suitable STED pulses, with pulse energies of up to $5nJ$ in $1ns$, are obtained from a second semiconductor laser system. Based on a tapered amplifier, this system is constructed to be operated flexibly in various modes of ns pulse generation. With this semiconductor STED laser subdiffraction imaging of fluorescent nuclear track detectors is successfully performed for the first time. Thereby the size of tracks of carbon ions and protons in this material can be determined.
Furthermore, a method for all-semiconductor picosecond-pulse generation at wavelengths of $532nm$, 561 and $593nm$ is presented. This was so far not possible and provides a convenient source of excitation light for red emitting organic dyes, not only for STED nanoscopy.
With its findings this thesis proves that STED imaging with a fivefold resolution enhancement is possible with user-friendly and affordable lasers. This paves the way to a wide spread use of STED nanoscopy.

Zusammenfassung

Seit die STED Nanoskopie vor zwanzig Jahren zum ersten Mal vorgeschlagen wurde, hat sich die Methode zu einem mächtigen Werkzeug der Fernfeld Fluoreszenzbildgebung entwickelt, mit dem Auflösungen unter $20nm$ möglich sind. Dennoch wird die breite Anwendung von STED in den Lebenswissenschaften vom hohen Aufwand, den die Methode mit sich bringt, behindert. Dieser Aufwand ist zum großen Teil durch den STED Laser begründet. Die bisher für STED verwendeten Laser, z.B. Titan-Saphir Laser, weisen sowohl technische, als auch praktische Unzulänglichkeiten auf, was zu komplexen Nanoskopie Systemen führt.
Halbleiterlaser, die kompakt, zuverlässig und ohne Aufwand ansteuerbar sind, stellen eine ideale Möglichkeit dar, um diese Situation zu verbessern. Daher untersucht diese Arbeit das Potential verschiedener Halbleiterlaserarchitekturen

im Hinblick auf STED. Fabry-Pérot Laserdioden im übersteuerten gewinngeschalteten Betrieb werden als geeignete STED laser präsentiert. Pulse mit Energien von $5nJ$ in $1ns$, die noch besser für STED geeignet sind, werden von einem weiteren aufgebauten Halbleiterlaser-System erzeugt. Dieses System, das auf einem Trapezverstärker basiert, ist so konstruiert, dass es flexibel in verschiedenen Modi der Nanosekunden-Pulserzeugung betrieben werden kann. Mit diesem Halbleiter STED Laser ist es zum ersten Mal möglich, Bildgebung jenseits der Beugungsgrenze an fluoreszenten Partikelspurdetektoren durchzuführen. Dadurch kann die Größe von Kohlenstoff- und Protonenspuren in diesem Material vermessen werden. Darüber hinaus wird eine neuartige halbleiterbasierte Laserquelle für Pikosekunden-Pulse bei Wellenlängen von $532nm$, $561nm$ und $594nm$ vorgestellt. Diese eignet sich hervorragend als Lichtquelle zur Anregung für rot emittierende Farbstoffe, nicht nur für STED.
Mit ihren Erkenntnissen belegt diese Arbeit, dass benutzerfreundliche und erschwingliche Laser für STED Nanoskopie mit fünffacher Auflösungserhöhung benutzt werden können. Dies ebnet den Weg hin zu einer breitgestreuten Anwendung der STED Nanoskopie.

Contents

Symbols & Acronyms

$[a.u.]$	Arbitrary units
I	Light intensity $[W/m^2]$, electrical current $[A]$
I_{max}	Maximum light intensity
I_{peak}	Peak value of an electrical current pulse
λ	Wavelength of light
ν_L	Laser pulse repetition rate
n	Index of refraction
NA	Numerical aperture, $NA = nsin\alpha$
τ_p	Laser pulse length
TEM_{00}	Fundamental Gauss-Laguerre mode of the transverse electromagnetic field
APD	Avalanche photodiode
ASE	Amplified spontaneous emission
BAL	Broad area laser
CLSM	Confocal laser scanning microscope
COD	Catastrophic optical damage
CW	Continuous wave
DBR	Distributed Bragg reflector
DC	Direct current
DFB	Distributed feedback
DPSS	Diode pumped solid state
FNTD	Fluorescent nuclear track detector
FOV	Field of view
FP	Fabry-Pérot
FWHM	Full width at half maximum
GY-gap	Green-yellow gap

LASER	Light amplification by stimulated emission of radiation
LD	Laser diode
LED	Light emitting diode
LSM	Laser scanning microscope
MOPA	Master oscillator power amplifier
MOSFET	Metal-oxide-semiconductor field-effect transistor
OI	Optical isolator
PBS	Polarizing beam splitter
PCB	Printed circuit board
PD	Photodiode
PMF	Polarization maintaining fiber
PMT	Photo multiplier tube
PPLN	Periodically poled $LiNbO_3$
PSF	Point spread function
RW	Ridge waveguide
SC	Semiconductor
SHG	Second harmonic generation
SLD	Superluminescent diode
SM	Single mode
SMF	Single mode fiber
SOA	Semiconductor optical amplifier
SPICE	Simulation Program with Integrated Circuit Emphasis
STED	Stimulated emission depletion
SWP	Segmented waveplate
TA	Tapered amplifier
TC	Two-contacts
TEC	Thermoelectric cooler
TL	Tapered laser
TTL	Transistor-transistor logic
VPP	Vortex phase plate

Introduction

1

The impossible is sometimes only impossible in people's minds. When Columbus made a round egg stand on its tip, he proved that with a suitable approach an impossible thing can become possible without changing any conditions. Similarly, the diffraction limit in optical imaging could be overcome although light is still subject to diffraction. Nevertheless, the diffraction limit was an insurmountable limitation for more than 120 years.

In 1873 Ernst Abbe found out that the resolution of an imaging system is fundamentally limited by the diffraction of light to about half the wavelength λ, of the light [1]. For visible light, i.e. $\lambda = 400nm$ - $700nm$ this yields resolutions of about $200nm$. The diffraction limit applies in particular to optical far-field microscopy, where resolution is one major factor of high image quality. Since microscopical methods are heavily used in the life sciences, the diffraction limit was not only a limitation to itself, but also limited the insight which could be gained from microscopical studies. Technical progress during the 20^{th} century allowed for microscopes which came very close to diffraction limited imaging even with large fields of view and over a large wavelength range. Especially fluorescence microscopy and confocal microscopy enabled microscopy images which were merely limited by diffraction [2]. The development of structured illumination microscopy and 4-pi microscopy allowed to shift the diffraction limit of such microscopes to slightly lower values, without fundamentally breaking it, though [3, 4]. Therefore, every cellular structure smaller than $100nm$ remained veiled by diffraction. Simultaneously methods which can image with better resolutions had been developed. Near-field microscopes, atomic force microscopes and electron microscopes yield resolutions down below $1nm$ [5–7]. However, these techniques are essentially restricted to surfaces, which limits their benefit for biological studies. Especially the possibility of life cell and in depth examination of biological tissue is reserved to far-field imaging.

The key to overcoming the diffraction limit in optical far-field microscopy was to take the attention off the classical picture which only takes into account wave nature of light. In this picture a microscopy sample is not regarded to be capable of taking any influence on the imaging process. As a matter of fact, the sample does provide what is necessary to fundamentally break the diffraction limit. Its quantum mechanical molecular structure can be exploited for this purpose. The first method

to do so was proposed exactly twenty years ago [8]. It is called stimulated emission depletion (STED) microscopy and relies on reversible switching between molecular states by absorption and stimulated emission of photons. It was soon perceived that there are other mechanisms which also enabled breaking of the diffraction barrier by the switching approach [9]. Nevertheless, STED was the first far-field microscopy technique to produce diffraction unlimited images [10, 11]. Other techniques followed. Ground state depletion microscopy (GSD), photoactivated localization microscopy (PALM), stochastic reconstruction microscopy (STORM), and variants thereof have lead to a zoo of techniques for diffraction unlimited far-field microscopy, which was termed optical nanoscopy [12–14]. By now optical nanoscopy is being performed with many classes of fluorophores, and reaches resolutions below $20nm$ in biological tissue [15–17]. Resolutions beyond the diffraction barrier have also been obtained from living biological samples and even in a living mouse [18, 19].
Now that the limitation by diffraction has obviously been abolished, what remains to be done? Unlike Columbus' idea of flattening the egg's tip, the realization of STED nanoscopy did not come without effort. Although the method has been demonstrated to work very well and, from a life scientist's point of view, fulfills many requirements, its application is often hindered by its complexity and cost. The difference between a STED nanoscope and a confocal scanning microscope is basically only one laser which has to be added, the so-called STED laser. Unfortunately there are several reasons why it is this laser which introduces complexity to the method. STED nanoscopy makes unique demands on its lasers, regarding the combination of pulse length, pulse repetition rate and pulse energy. Therefore, complex lasers such as Titanium-Sapphire (Ti:Sa) lasers or optical parametric oscillators (OPO) seemed to be the only lasers meeting these requirements [20–22]. Upon employing these lasers there were new challenges to cope with. Shaping the spatial and temporal beam properties had to be performed and synchronization of laser pulses required laborious solutions. Due to these circumstances the overall effort which had to be invested in order to obtain a reliable STED nanoscope was immensely high when compared to conventional microscopy methods. Obviously, a STED laser which would also meet practical requirements was highly desirable. Consequently, the work leading to this thesis aimed at finding alternative high performance STED laser architectures. In many respects, the most attractive laser type is the semiconductor laser. It combines small size, low cost and reliability, and can be controlled and operated more flexibly than any other laser type [23]. If a laser which combines these advantages could be adapted to meet the pulsing requirements of STED, the method could greatly benefit. Better handling and lower effort in acquisition and implementation would hugely promote the availability of STED nanoscopy to the life scientific community, such that its potential could be

fully exploited. Therefore, based on a study which has been carried out with laser diodes as STED lasers [24], this thesis investigates the potential which semiconductor lasers bear when used as STED lasers. For this purpose semiconductor laser systems of different architectures have been tailored to meet the demands of a STED laser, and were tested in a STED nanoscope.
This thesis is outlined as follows. The first chapter introduces the basic concepts of STED, particularly those methodical details which were implemented in the experiments. Then a chapter is dedicated to the description of nanosecond pulsed semiconductor lasers. Two semiconductor STED laser systems are presented. Furthermore, based on the work on STED lasers, a novel semiconductor excitation laser source in the green-yellow spectral range will be presented. Chapter 4 presents the results which could be obtained by including the presented lasers into STED nanoscopes. Finally, the results will be discussed and lead to an outlook as to future utilization of semiconductor lasers in STED nanoscopy.

STED Nanoscopy

2

The outstanding advantage of STED nanoscopy over conventional microscopy methods is its theoretically unlimited resolution [8, 25, 26]. This potential has made STED nanoscopy an important tool of nanoscale imaging based on far field fluorescence microscopy. This chapter gives a brief introduction to the fundamentals of STED nanoscopy. To start off, an explanation of the diffraction barrier will be given. Section 2.2 introduces the concept of fluorescence microscopy and explains how STED nanoscopy outstrips the diffraction barrier. STED-related techniques which have come up more recently and will be important in the course of this thesis are introduced in sections 2.3 and 2.4 . The role and the requirements of lasers for STED will be highlighted in 2.5 .

2.1 The Diffraction Barrier

Before the invention of STED nanoscopy, all techniques of light microscopy were fundamentally limited in resolution due to the diffraction of light. This limitation was dubbed diffraction limit or diffraction barrier. Due to the fundamental significance for the field of diffraction unlimited microscopy, a brief motivation for the origin of the diffraction is presented. The interested reader is referred to the literature for a more detailed discussion of the matter [27–29].
An elaborate version of the presented approach can be found in [30]. Consider a stationary monochromatic wave $U(x, y, z)$ of wavelength λ, and wavevector $\vec{k} = (k_x, k_y, k_z)$ with

$$k = |\vec{k}| = \frac{2\pi}{\lambda}, \quad k_z = \pm\sqrt{k^2 - k_x^2 - k_y^2} \tag{2.1}$$

This wave can be expressed as a superposition of plane waves, $\exp(-i\vec{k}\vec{r})$:

$$U(x, y, z) = \frac{1}{2\pi} \iint F(k_x, k_y) e^{-ik_z z} e^{-i(k_x x + k_y y)} \, dk_x \, dk_y \tag{2.2}$$

where $F(k_x, k_y)$ provides the amplitudes of the plane waves. Note that the shape of U in the x-y-plane at $z = 0$ is given by the Fourier transform of $F(k_x, k_y)$.

Propagation along the z-direction is described by the term $\exp(-ik_z z)$. Due to relation (2.1) the exponent of this so-called propagator can become real for certain wavevector components k_x and k_y, which do not fulfill

$$k_x^2 + k_y^2 < \frac{(2\pi)^2}{\lambda^2}. \tag{2.3}$$

The contribution of these k_x and k_y is attenuated during propagation[1]. The shape of U in the x-y-plane at $z = d$ is then given by the Fourier transform of $F(k_x, k_y) \cdot \exp(-ik_z d)$, such that the k_x and k_y which are prohibited by (2.3) do not contribute in the far-field, i.e. for $d \gg \lambda$. That means there are maximum k_x and k_y which shape the far-field intensity distribution of the propagating wave. In other words, this intensity distribution has a minimum extent which cannot be reduced any further, known as the diffraction limit.
This approach motivates the existence of the diffraction limit. It is very general, though, and was derived irrespective of any optical elements involved. Still, the approach is suitable to make the following point. The diffraction limit originates from the wave properties of light. A wave of light can only be focused down to a certain limit, which is given by its wavelength. When the transition to a real optical system is made, the medium in which the light propagates with refractive index n is introduced as well as a maximum angle α at which the light field can access the utilized optics, which further restricts condition (2.3). This culminates in the well-known formulation of the resolution limit Δx of an optical system using the wavelength λ and numerical aperture $NA = n \sin \alpha$

$$\Delta x = \frac{\lambda}{2NA}, \tag{2.4}$$

which was introduced by Ernst Abbe in 1873 [1].

2.2 STED Fundamentals

Fluorescence Micorscopy

The fundamentals described below and an extensive treatment of confocal microscopy in general can be found in [31]. Fluorescence microscopy is among the most widely used microscopy techniques in life science research. It requires the sample to be stained with a fluorescent dye. Labeling of the structure under examination provides huge advantages over label-free microscopy. It enables highly specific and high contrast imaging of the stained features. The most basic implementation of a STED nanoscope is based on a fluorescence microscope, more

[1] From relation (2.1) ther is also a solution for k_z leading to an amplification which is, however unphysical and is therefore neglected.

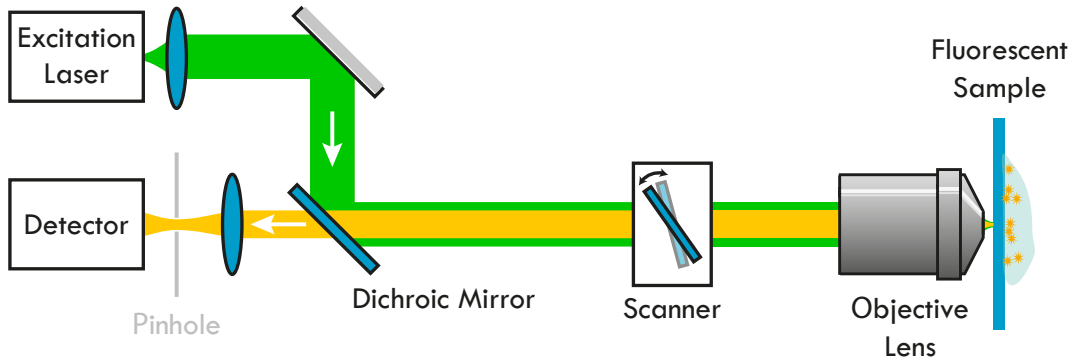

Figure 2.1.: Schematic laser scanning microscope (LSM). Adding the pinhole converts the LSM into a confocal LSM, which delivers the best diffraction limited resolution. An LSM can be upgraded to a STED nanoscope.

precisely on a laser scanning microscope (LSM). Therefore, it is necessary to shortly introduce this kind of microscope. A sketch of an LSM is shown in figure 2.1. It comprises a laser source which is apt to generate a fluorescence signal in the sample. The laser light is focused into the sample by an objective lens, which, at the same time, is used to collect the emitted fluorescence. The fluorescence signal is then separated from the illumination beam path by a beam splitter, and is guided to the detector. Due to the Stokes-shift (cf. figure 2.2) between the excitation and emission spectra, which is characteristic of organic dye molecules, a dichroic mirror is the easiest way to realize such a beam splitter. The detected signal value can be assigned to a certain image pixel. Adding a scanning unit makes it possible to acquire signal values from a certain field of view (FOV) within the sample, thus reconstructing an image of this region of the sample. Scanning can be implemented in two ways. Either the sample can be moved with respect to the illuminating beam or the laser beam can be steered to scan the sample.
The contrast and the axial resolution is further improved if a pinhole is placed in front of the detector. This pinhole efficiently filters out fluorescence which does not originate from the focal plane of the objective lens. Such a kind of microscope is called confocal laser scanning microscope (CLSM) and reaches the best diffraction limited resolutions. It is fundamentally limited by diffraction, as described in 2.1. The diffraction limit is present at two stages of the CLSM. It limits the size of the laser spot to a minimum extent, yielding the illumination point spread function (PSF) h_{ex}. Also, the emitted fluorescence light is subject to diffraction, its imaging onto the detector is expressed by the detection PSF h_{det}. The multiplication of the illumination and detection PSF gives the total PSF

$$h = h_{ex} \cdot h_{det}. \tag{2.5}$$

In this work, the full width at half maximum (FWHM) of h will be used as a measure for the resolution Δx of a given microscopy system.

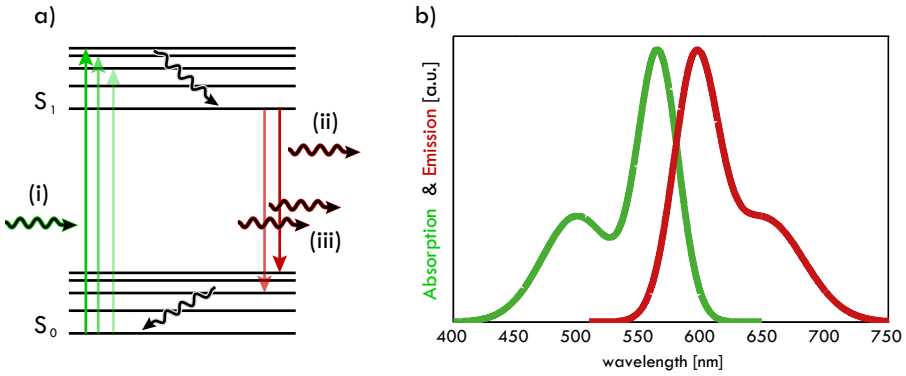

Figure 2.2.: Characteristics of a typical organic dye. The Jablonski diagram, a), schematically shows the relevant energy level structure of an organic dye. The three radiative processes are excitation (i), spontaneous emission with $\tau > 1ns$ (ii) and stimulated emission (iii). The transitions between sub states within S_0 and S_1 with $\tau < 10ps$ are responsible for the energy loss between absorption and emission, resulting in the so-called Stokes-shift. This can be seen clearly in the spectrum of the transition, b) [32].

The STED Principle

Throughout the past two decades the fundamentals of STED nanoscopy have been discussed extensively [33–35]. Therefore, only a brief explanation of the principle will be given here. In the preceding discussion of a CLSM the illumination light provides the main contribution to limiting the resolution. This description concludes that features which are illuminated at the same time, cannot be resolved by a scanning microscope. At a closer look, however, this is only true if the different features also respond to illumination at the same time. This thought introduces another important part of the microscope system, which is the sample under examination itself and its response to illumination. If a mechanism can be found, which introduces a spatial dependence in this response on a subdiffraction-sized-scale, discrimination between responding and non-responding subsets becomes possible, irrespective of their distance. Sequential probing of different feature subsets within a diffraction limit sized volume thus enables subdiffraction imaging. In the case of fluorescence microscopy, the excitation laser can be considered to switch the dye from the ground state (*off*) into the excited state (*on*). In this picture, subdiffraction imaging requires the reverse switching mechanism, i.e. switching from *on* to

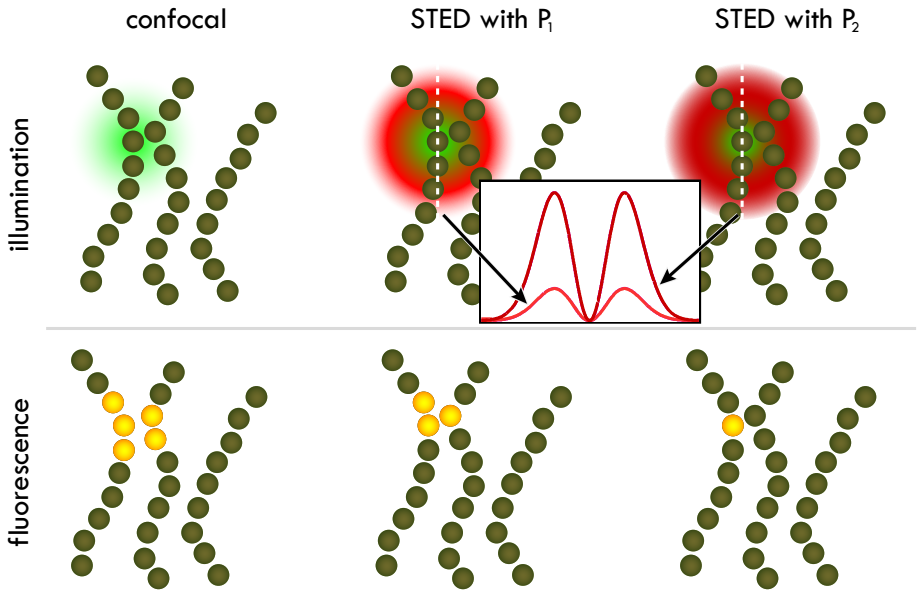

Figure 2.3.: The principle of STED. Switching some of the excited fluorophores *off* leaves a smaller region to contribute to the signal of each pixel. The inset shows the diffraction limited STED patterns along the dashed lines. By scaling the STED laser power up the *on* volume can in principle become arbitrarily small.

off, where the dye's ability to fluoresce is reversibly disabled. Stimulated emission provides such an off-switching mechanism. Stimulated emission was postulated by Einstein [36, 37] as the field dependent transition from a high energy quantum state to a lower one. It contrasts spontaneous emission, which is independent of external fields. These three processes are exploited for switching and signal generation in STED nanoscopy.
As mentioned in the context of fluorescence microscopy, organic dye molecules exhibit a red shift of their emission spectrum relative to the absorption spectrum, the Stokes-shift. The difference in energy is lost via relaxation of vibronic sub-states of the excited electronic state prior to spontaneous emission, cf. figure 2.2 . The Stokes shift is essential for the molecular switching in STED. Without the shift, a laser which induces stimulated emission would also be capable of exciting the dye, leaving no distinct on- and off-switching mechanisms. Consequently, STED nanoscopy, in addition to the excitation laser, makes use of a second laser. This STED laser has a red shifted wavelength as compared to the excitation laser, and is thus capable to switch dyes off. Furthermore the beam profile of this laser is manipulated such that within the focused beam profile there is at least one point of zero intensity. At this point, and in its close vicinity, no stimulated emission can take place, leaving a subset of the excited molecules in the on-state. Due to the

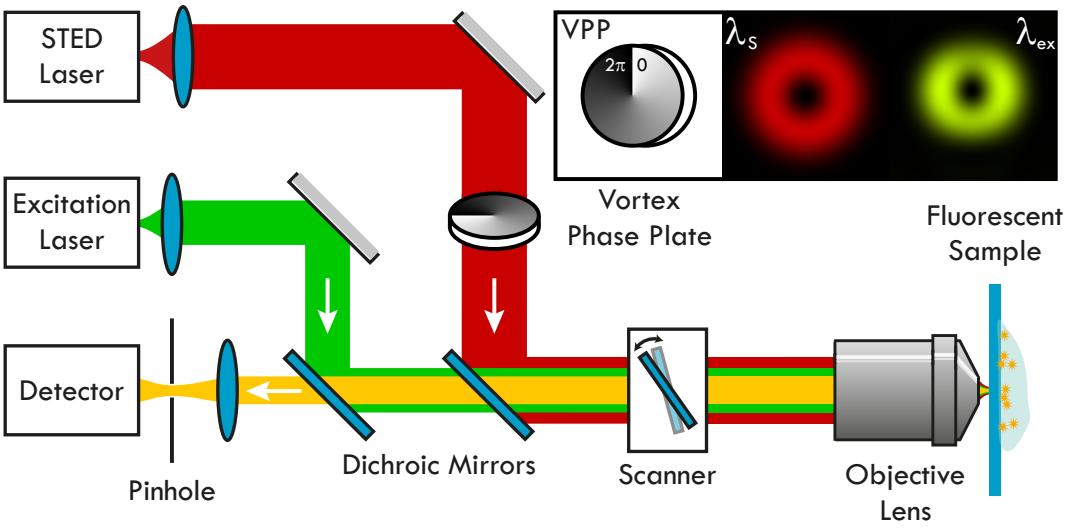

Figure 2.4.: Schematic conventional STED setup. After phase modulation of the STED beam, the laser beams are overlaid, scanned and focused into the sample. Dichroic mirrors are utilized to filter the fluorescence out of the laser beam path. The beams have to be overlaid after phase manipulation by the VPP. The reason for this is shown in the inset, the VPP would also generate a central intensity minimum in the excitation beam.

intensity dependence of stimulated emission, in regions of increasing STED intensities the probability to find excited molecules is lowered. Although the STED beam pattern is also inevitably diffraction limited, the off-switching can be performed with high probability arbitrarily close to an intensity zero. Thereby the volume within which excited molecules can reside can become significantly smaller than the diffraction limited volume. Since only this reduced volume contributes to the signal at each probing interval, in effect the resolution is improved by this scheme. In figure 2.3 the STED principle is illustrated for the typical case of a doughnut shaped STED beam. The resolution of such a STED nanoscope is approximated by adding a factor to the Abbe formula (2.4).

$$\Delta x \propto \frac{\lambda}{2NA} \cdot \frac{1}{\sqrt{1 + \frac{I_{max}}{I_{sat}}}} \tag{2.6}$$

This popular formula for Δx employs the maximum intensity of the STED pattern I_{max} and introduces the saturation intensity I_{sat}, which is a measure for the intensity which is needed for off-switching. Utilization of the intensity, however, can be misleading, as will be discussed now. Indeed, the probability density, k_{st}, for stimulated emission of a molecule does depend on the intensity I of the incident

light [37].

$$k_{st} = \frac{I}{h\nu}\sigma(\nu), \tag{2.7}$$

where $h\nu$ is the photon energy and $\sigma(\nu)$ the cross section for stimulated emission. To find a definite probability from this, the interaction time has yet to be defined. In the case of a pulsed STED laser the interaction time is the pulse length τ_p. This is accounted for by I_{sat} which depends on τ_p according to [38]

$$I_{sat} = ln2\frac{h\nu}{\sigma\tau_p}.\ ^{2} \tag{2.8}$$

Therefore, if only the intensity of the STED laser is known, the possible resolution enhancement cannot yet be estimated. This is especially important when lasers of different pulse lengths are compared. A more general expression can be found if the laser pulse length is taken into account, such that the pulse energy

$$E_p = \iint I(x,y,t)\ dA\ dt = I_{max} \cdot \tau_p \cdot A \tag{2.9}$$

substitutes I_{max}, with the the beam cross section A. Using equation (2.6), this leads to

$$\Delta x \propto \frac{\lambda}{2NA \cdot \sqrt{1 + \frac{E_p}{E_{sat}}}}, \tag{2.10}$$

where the saturation pulse energy is now given by

$$E_{sat} = I_{sat}\tau_p A \propto h\nu\frac{\lambda^2}{\sigma NA^2}, \tag{2.11}$$

since $A \propto (\lambda/NA)^2$. In other words, the ratio of λ^2/σ approximately gives the number of photons in a pulse of energy E_{sat}. This is valid for any laser, as long as τ_p lies within the range $10ps$ - $3ns$, which will be discussed in more detail in 2.4 . Most importantly equations (2.6) and (2.10) show that, given enough STED photons are available, the resolution of a STED nanoscope does not have a lower boundary.

2.3 easySTED

The generation of the STED intensity pattern is a key issue in the design of a STED setup [10, 39]. The most popular method so far utilizes a so-called vortex

[2] The form $I_{sat} = 1/\tau_p\sigma$ is mostly found. It refers to the photon flux density $[s^{-1}m^{-2}]$ at which fluorescence has reduced to $1/e$, whereas the formualtion used here gives the Intensity $[Wm^{-2}]$ at which fluorescence has dropped to half its value.

phase plate (VPP) [40–42]. It is a polymer plate of which one surface is structured with a spiral. The dimensions of the spiral are chosen such, that the optical path difference at the spiral step equals the STED wavelength λ_S. If a laser beam passes through the plate with its center at the spiral center, opposing regions of the beam profile acquire a phase difference of π (i.e. $\lambda/2$). Focusing this beam then leads to destructive interference at the very center of the focal spot, yielding the desired doughnut shape. After generating the STED intensity pattern the STED beam is overlaid with the excitation beam, since in the profile of the latter a central intensity maximum has to be maintained, cf. figure 2.4 .
In the attempt of enabling more rugged and compact STED setups, an alternative method to using the VPP has been developed recently, dubbed easySTED [43]. Instead of introducing phase differences by optical path differences, the easySTED approach manipulates the polarization of the light. Rotating the polarization of linearly polarized light by an angle of $\varphi = \pi$ also yields a beam with a phase difference of π with respect to the unrotated beam. An optical element performing this rotation of $\varphi = \pi$ is called a half-wave-plate ($\lambda/2$-plate), which is based on a birefringent material [30]. With the help of half-wave-plates an intensity pattern similar to the vortex doughnut can be generated. To this end four $\lambda/2$-plates are arranged to form one segmented waveplate (SWP), cf. figure 2.5 . Neighboring plates have their fast axes oriented at an angle of $\pi/4$ with respect to each other. This assures that an incident polarized beam will have a polarization rotation of $\varphi = \pi$ in opposing regions of the beam profile, again yielding an intensity zero in the beam center when focused. The number of four segments is chosen more out of practical reasons than for necessity. Any number of segments $j > 2$ would give a central zero if the relative angle of the axes of neighboring plates is π/j. The radial symmetry becomes better for higher j. Four segments are especially simple to manufacture and arrange. They generate a characteristic clover leave-like intensity distribution. Nevertheless, the distribution close to the intensity zero shows very good radial symmetry, such that the beam profile is in good approximation

$$I(r) = I_{max}\frac{r^2}{a^2}e^{1-\frac{r^2}{a^2}}, \qquad a^2 = \frac{1}{5}\frac{\lambda^2}{NA^2}. \tag{2.12}$$

This doughnut generation scheme does not only work with a zero order $\lambda/2$-plate, but in fact for any rotation angle fulfilling $\varphi = (m \cdot 2 + 1)\pi$, where m is an integer. With increasing m the chromacity of the device becomes more pronounced, i.e. φ deviates increasingly for wavelengths λ_{ex} other than the design wavelength λ_S. For a certain λ_{ex} and a correctly chosen combination of the birefringent material and m, $\varphi(\lambda_{ex}) = (m \cdot 2 + 2)\pi$ becomes valid. For this λ_{ex} the SWP has no effect, because opposing regions in the beam focus to constructive interference. This gives rise to an alternative optical beam path design in a STED nanoscope. The beams of excitation laser and STED laser can be overlaid before the phase front

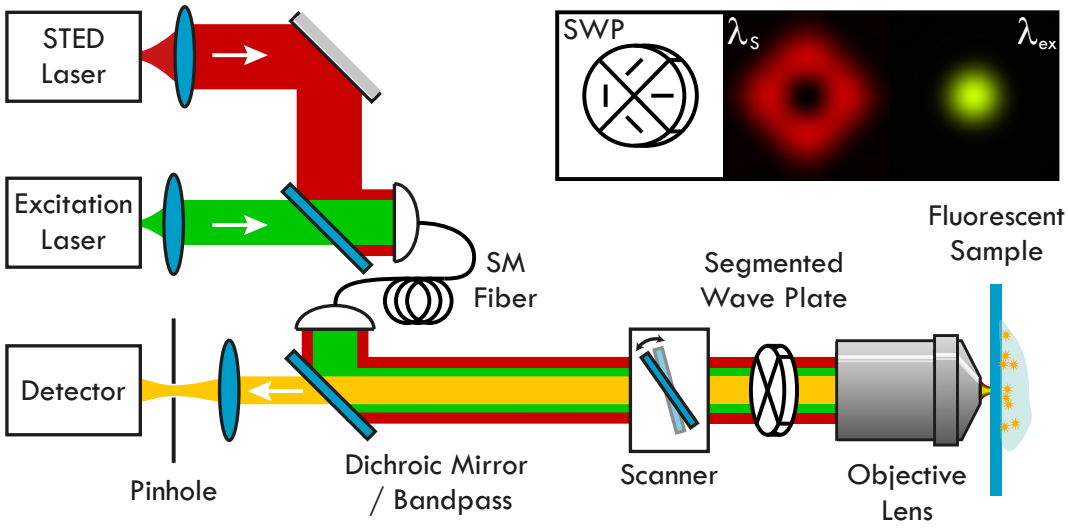

Figure 2.5.: Schematic setup of an easySTED nanoscope. The inset shows an SWP - the lines indicating the orientation of the fast optical axis of each 2.5 wave plate - and the resulting focal intensity distributions of the STED beam and the excitation beam, respectively. This enables joint transmission of the two beams through the SWP. Thus a single mode fiber can be employed for stable diffraction limited overlaying of the laser beams.

manipulation, e.g. by coupling them into a single mode fiber (SMF). This enables stable co-alignment of the two beams on a diffraction-limit scale. After overlaying the beams they can both pass through the SWP, where the STED doughnut phase pattern is generated, while the excitation beam maintains its gaussian shape. The SWP can then be placed in a conjugate plane of the back focal plane of the objective lens which is close to the objective lens itself. Placing it directly behind the objective lens, close to its pupil, avoids relay optics further down the beam path. This enhances compactness and stability of the optical system even more, enabling virtually alignment free STED nanoscopes [44].
A further difference between VPP and SWP implementations concerns the sensitivity to wavelength and polarization, which can affect the quality of the intensity zero. A high quality zero is crucial for a high resolution. If the ratio $I(r=0)/I_{max}$ is larger than about one percent severe signal loss at the doughnut center is the result. The wavelength of a VPP shaped STED beam can lie within a spectral range of up to $20nm$, without significant deterioration of the doughnut zero. The polarization, in contrast, has to be very clean and must be of only one circular orientation. A doughnut produced by an SWP , on the other hand, has to have a wavelength differing no more than 3 - $5nm$ from the design wavelength, while any

polarization is acceptable [45]. As a consequence, a certain STED laser requires a specially manufactured SWP. Furthermore, of a linearly polarized laser type, the beams of two identical units can be merged if they are arranged such that their polarizations are crossed. This provides a simple way to double the STED laser power. Such an easySTED setup will be presented in chapter 4 .

2.4 Time Gated STED

In addition to the patterning of the STED beam, the temporal sequence of the laser pulses and their respective lengths play a major role for the performance of a STED setup. There are mainly two time constants which determine STED laser timing. One is the relaxation constant of the vibronic states $\tau_{vib} = k_{vib}^{-1}$, which is on the order of ps, the other is the fluorescence lifetime $\tau_s = k_s^{-1}$, which for organic dyes is typically $\tau_s \approx 2$ - $3ns$. Processes taking place in the system have to be considered on these timescales. For STED the existence of the vibronic substructure is crucial in order to make the dye immune to excitation by the STED laser. If the rate at which excitation by the STED laser takes place $k_{st}^*(I_{STED}) > k_{vib}$, the process can still play a role, though. This would require immense $I_{max} \gg 10^9 W/cm^2$ and has not been reported to be an issue, unless fs laser pulses are used [46]. It will be neglected in the following considerations. Given a (rectangle) STED laser pulse of duration τ_p, the population of the S_1 state, N, and the number of subsequently spontaneously emitted photons, n, can be found by solving the rate equations [47]

$$\frac{dN}{dt} = \begin{cases} -k_s N - k_{st} N, & 0 < t \leq \tau_p \\ -k_s N, & \tau_p < t. \end{cases} \tag{2.13}$$

$$\frac{dn}{dt} = k_s N(t) \tag{2.14}$$

This shows that the STED shortens the effective lifetime of S_1. In the following treatment it will be assumed, that the population $N_0 = N(t = 0)$ was instantaneously established. In the experiment this is approximately fulfilled by employing an excitation laser with $\tau_p^{ex} \ll \tau_s$, typical excitation lasers have pulse lengths is in the range of $50ps$ - $100ps$ (see chapter 4). To find an expression for $n(t)$, (2.14) can be integrated directly. With some foresight to time gating this will be done starting at time t_g until the end of the pulse period $T = 1/\nu_L$.

$$n(t_g, T) = k_s \int_{t_g}^{T} N(t) \tag{2.15}$$

$$= \begin{cases} N_0 \left(\frac{k_{st}}{k_t} e^{-k_t \tau_p} + \frac{k_s}{k_t} e^{-k_t t_g} - e^{-(k_s T + k_{st} \tau_p)} \right), & 0 < t_g \leq \tau_p, \\ N_0 \, e^{-k_{st} \tau_p} \left(e^{-k_s t_g} - e^{-k_s T} \right), & \tau_p < t_g, \end{cases}$$

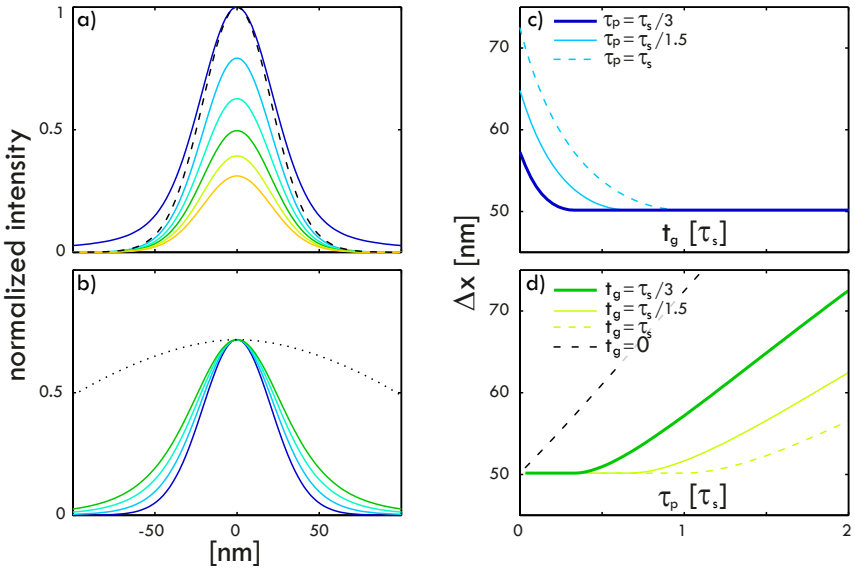

Figure 2.6.: Simulation of time gated detection. These simulations are based on (2.16), the pulse energy E_p is constant for all cases. a) pulse width $\tau_p = 1ns$, detection gate delay, t_g, is variable. The dashed line gives the optimum case of $\tau_p \ll \tau_s$ (fluorescence lifetime) and $t_g = 0$. For the other curves t_g is 0, $0.7ns$, $1.4ns$, $2.1ns$, $2.8ns$ and $3.6ns$ (blue to orange). Note the exponential signal loss with larger t_g. The difference to the width of the ideal case is only obvious for $t_g = 0$, for larger values the difference vanishes, as can also be seen in c). b) $t_g = 1ns$, τ_p is $0.1ns$, $3ns$, $4.5ns$ and $6ns$ (blue to green). The dotted line gives the confocal PSF. c) and d) Interplay of gating and pulse width, and their effect on Δx. It is important to notice that according to this treatment the optimum resolution for a certain E_p can always be recovered, irrespective of the STED pulse length. This is only possible, of course, at the cost of signal loss.

where, for brevity, $k_t = k_s + k_{st}$ was introduced as the total decay rate. The laser repetition rate ν_L is ideally chosen such, that all excited molecules emit within one laser cycle, i.e. $k_s T \gg 1$. Although these expressions were derived for an ensemble of fluorophores, they will also hold true for a single molecule when averaging over many laser cycles. Consequently, the signal after starting detection at t_g amounts to

$$n(t_g) = \begin{cases} N_0 \left(\frac{k_{st}}{k_t} e^{-k_t \tau_p} + \frac{k_s}{k_t} e^{-k_t t_g} \right), & 0 < t_g < \tau_p \\ N_0 \; e^{-k_{st} \tau_p} e^{-k_s t_g}, & \tau_p \leq t_g. \end{cases} \tag{2.16}$$

From this relation, the requirements for the pulse timing and the possibilities of time gating can be derived. It is important to remember that according to (2.7) k_{st} depends on the STED laser intensity $I(x, y)$ which, in turn, has a spatial

dependence. Consequently, where k_{st} contributes notably to one of the above equations, a spatial dependence is introduced to the temporal photon emission characteristics, as well. First, consider the case of $\tau_p \ll \tau_s$. Only the second case of (2.16) has to be considered then. Thus, the spatial signal distribution is fixed by $k_{st}\tau_p$, and does not depend on t_g. This is the ideal case for STED, for which $t_g = 0$ can be chosen without any trade-off. All photons arriving at the detector are collected.
If, on the other hand, τ_p is of a similar order as τ_s, the first case has to be considered as well. Then the signal contains photons, which are emitted from regions where $I > I_{sat}$ while the STED laser beam is on. One can consider these photons as a diffraction limited, thus undesired, contribution to the total signal. That is why it becomes interesting not to detect all photons arriving at the detector. This can be done by the help of the time gate defined in (2.16), between t_g and the next excitation pulse. The effect of using such a detection time gate is shown in figure 2.6. It illustrates that if $t_g = \tau_p$ the optimum resolution can be recovered, which can also be seen from equation (2.16), since that means only applying the second case. The graphics imply that if time gated detection is employed, the obtainable resolution only depends on the pulse energy of the laser, and not on the pulse length. A drawback of the time gated mode is that not only unwanted photons are filtered out of the signal. Since the desired signal decays with τ_s, STED pulse lengths shorter than τ_s are still favorable. If by stretching the pulses the pulse energy is increased, thus enabling higher resolutions, a compromise between photon yield and gating has to be found.
So far time gating has mainly been used in combination with CW STED, meaning that a continuous wave STED laser was utilized [48–50]. This corresponds to the extreme case of $\tau_p = \tau_s$, therefore it is clear that resolution and contrast can profit considerably from time gated detection. Since lasers have come up which feature pulses with $\tau_p \approx 1ns$, however, gating has also become popular for pulsed STED [17].

2.5 Lasers in STED Nanoscopy

In the previous sections state of the art developments for optics and signal capture in STED nanoscopy have been introduced. This section discusses the role of lasers for STED and gives examples for commonly used lasers. Data will be quoted concerning the requirements for excitation lasers and STED lasers, respectively. It will be used as benchmark in the following chapters, which has to be fulfilled or approached by semiconductor lasers to promise proper performance in a STED nanoscope. Only pulsed lasers are considered.
Important laser parameters for STED are the wavelength λ and the bandwidth $\Delta\lambda$;

the state of polarization; the beam quality, measured as M^2; the pulse repetition rate ν_L; the pulse energy E_p and the pulse width τ_p. So far for the quantitative physical characterization. Besides that practical considerations e.g. reliability or expense of a laser are important issues, and will be a matter of discussion.
Furthermore, it should be mentioned that the performance of a STED nanoscope is crucially dependent on the combination of lasers and fluorophores. Consequently, the consideration of lasers only is not complete and the numbers quoted later on are related to popular well suited fluorophores.

2.5.1 The Excitation Laser

The availability of excitation lasers is barely a problem for STED. This is due to the fact, that the same lasers which are used for confocal microscopy or other fluorescence applications like fluorescence lifetime imaging and spectroscopy, can be employed. Most of their parameters are determined by the target fluorophores. The wavelength should be close to the dye's absorption maximum. Since typical dye spectra have widths of several $10nm$ the exact λ and $\Delta\lambda$ are not critical parameters. To be able to excite molecules of arbitrary dipole orientation, both polarization states have to be present in the excitation volume. This is mostly accomplished by generating circularly polarized light from a linearly polarized laser beam. The repetition period $T = 1/\nu_L$ has to be at least a few multiples of the fluorescence lifetime in order to make use of lifetime effects, like time gated detection. At the same time ν_L is ideally not more one order of magnitude lower than this maximum value to ensure fast photon collecting. The excitation pulse energy is given by the extinction ratio of the dye, typically it is in the pJ range. Favorably the pulse width is very short in comparison to τ_s, as explained in 2.4. In order to guarantee diffraction limited focusing $M^2 \approx 1$ is required, as emitted by spatial single mode (SM) lasers. Popular lasers fulfilling these requirements are gain switched laser diodes. In that sense semiconductor lasers are already present in STED microscopy. As far as semiconductor lasers for excitation are concerned, one issue remains: So far there are no laser diodes emitting between $525nm$ and $625nm$, an important excitation wavelength regime for red emitting dyes. This is often referred to as the green-yellow gap (GY-gap). For this wavelength region the utilization of e.g. white light fiber lasers is necessary. Precise numbers of the laser requirements and an exemplary excitation laser are quoted in table 2.1.

2.5.2 The STED Laser

Some of the requirements for a STED laser are similar or identical to those for the excitation laser. The repetition rate, has to be the same, of course, since a fixed relative timing of the two lasers at each pulse is required. The beam quality has to

	Exc. Laser		STED Laser		
	Ideal	Laser Diode	Ideal	Ti:Sa	
λ	630 - 640	635	760 - 780	750	nm
ν_L	10 - 100	1-80	10 - 100	80	MHz
τ_p	< 0.15	0.07	0.2 - 1.5	0.0002	ns
E_p	> 0.005	0.05	> 5	5	nJ

Table 2.1.: Laser requirements for STED. The values for the wavelength are specified for infrared dyes similar to STAR635P. Examples are given of widely used lasers for excitation and STED, respectively [51–53]. Note that the Ti:Sa laser features suitable values except for the pulse length which makes pulse stretching necessary.

be equally good for the both lasers. This requirement is even more strict for the STED laser, since the STED pattern generation requires minimum deformation of the wavefront.

Polarization

Like for the excitation, laser both polarization components of the STED laser are desired in the focus, in order to be able to switch off molecules of arbitrary dipole orientation [45]. Therefore, mostly circularly polarized light is used. Depending on the doughnut generation method, however, the demands on the degree of polarization differ, cf. 2.3. The vortex phase plate is polarization sensitive and works with only one circular polarization. An easySTED SWP in contrast is not sensitive to polarization such that any polarization can be utilized.

Wavelength Properties

The central wavelength of the STED laser has to be positioned on the red slope of the fluorophore emission spectrum. A compromise has to be found. Choosing a wavelength in the far red decreases the stimulated emission cross section, $\sigma(\lambda)$, while approaching the emission maximum bears the risk of re-excitation by the STED laser.
The bandwith, contrary to the polarization, is more critical when an easySTED SWP is used. As indicated in 2.3, then the maximum $\Delta\lambda$ is about $5nm$, whereas a VPP is very bandwidth tolerant.

Pulse Properties

The requirements concerning the pulse length τ_p of the STED laser have been discussed in 2.4. There is no strict upper limit for τ_p. Nonetheless the analysis has

shown that extending the pulse length beyond the fluorescence lifetime τ_s, only improves resolution at the cost of of signal, i.e. contrast. Therefore, here τ_s is used as upper pulse length limit. Unlike the excitation pulse, the STED pulse width has a lower limit, as was also discussed in 2.4 . It is on the order of $\tau_p \approx 1ps$ [46]. The essential parameter of the STED laser is the pulse energy, since it determines the resolution achieved by STED. According to equation (2.10), the resolution enhancement ξ can be approximated as

$$\xi = \frac{\Delta x(conf)}{\Delta x(STED)} \approx \sqrt{\frac{E_p}{E_{sat}}}. \tag{2.17}$$

The saturation intensity can be evaluated with the approximation for the doughnut shape, since then $A = e\ \pi a^2/5$. Inserting this into equation (2.11) yields

$$E_{sat} \approx 1.18 \frac{h\nu}{\sigma_{st}(\lambda)} \left(\frac{\lambda}{NA}\right)^2 = 1.18 \frac{hc}{\sigma_{st}(\lambda)} \frac{\lambda}{NA^2}. \tag{2.18}$$

For $\lambda = 660nm$, $NA = 1.4$ and $\sigma(\lambda) = 0.5 \cdot 10^{-16} cm^2$, which is typical for organic dyes, and a desired resolution enhancement of $\xi = 5$, relation (2.17) yields a pulse energy of about $E_p = 0.5nJ$, which has to be delivered into the focus. Depending on the complexity of the optical setup between laser source and objective lens, the losses can amount to 70% or more. The actually emitted pulsed energy has to be accordingly higher. Table 2.1 sums up the essential laser requirements for STED nanoscopy.

Pulsed Semiconductor Lasers and Laser Amplifiers

3

In the first days of its existence, more than fifty years ago, the laser was regarded a solution without a problem [54]. Even if such comments were not entirely serious, they show that at that time the potential of lasers was not fully conceived. As a matter of fact, applications for which lasers could be used emerged very soon. Nowadays lasers are almost ubiquitous in research, industry and every day life, and the range of applications is constantly being expanded. Accordingly, world wide laser revenues amount to billions of dollars each year, half of which is covered by laser diodes (LDs) [55].

In order for semiconductor (SC) lasers to become this successful several technical challenges had to be tackled. It had been conceived in the late 1950s, that certain semiconductors are suitable laser media [56, 57]. Consequently, only two years after lasing had first been demonstrated at optical frequencies [58], the first successful operation of a semiconductor laser was published [59, 60]. These first diode lasers, however, struggled with high threshold currents, so that they only worked in pulsed mode and at liquid nitrogen temperatures. The development of semiconductor heterostructures providing charge carrier confinement to a small volume marked a major step towards LDs as mass product. Refinement of this technology lead to the current standard of quantum well laser diodes and quantum dot lasers [57].

With their increasing maturity, diode lasers had fundamental influence on several branches. Telecommunication, for example, was revolutionized by the availability of both, laser diodes and glass fibers as optical transmission lines [61]. This was also a motivation for the development of semiconductor optical amplifiers (SOAs) since they could serve as buffers in long transmission lines [62]. Near-infrared LDs, red LDs and finally blue LDs paved the way of compact optical data storage with increasing capacities [63]. The remaining challenge by now is the development of green-yellow LDs, promising e.g. highly compact and efficient laser projectors and other display applications. The huge efforts involved in this sequence of technological innovations were driven by the promise of a light source with extraordinary properties. LDs combine small size, high efficiency, high reliability and fast modulation response to name but a few of these properties.

For the same reasons diode lasers became attractive scientific tools. Especially in the fields of spectroscopy and fluorescence imaging laser diodes are irreplace-

able [64, 65]. In these applications, the laser diode, often tuned to a distinct operating frequency, induces atomic or molecular transitions. In fluorescence microscopy diode lasers are used exactly in this way. There, especially the spatial single mode (SM) emission and the high frequeny modulation capability are important features, as described in chapter 2 .
The aim of this work was to explore the potential of semiconductor lasers for STED nanoscopy. Since laser diodes have already been established as excitation lasers, emphasis will be put on semiconductor STED lasers. If high performance semiconductor STED lasers were available, their advantageous features mentioned above could greatly enhance the availability of STED nanoscopy in life science research. After a short introduction of different semiconductor types (section 3.1), this chapter includes an analysis of the pulsing properties of Fabry-Pérot (FP) LDs in 3.2. In section 3.3 a semiconductor master oscillator power amplifier (MOPA) system will be presented which delivers powerful ns pulses. In addition to this analysis of STED lasers, section 3.4 presents a novel type of semiconductor excitation laser, which bridges the green-yellow gap.

3.1 SC Laser Types & Pulsing

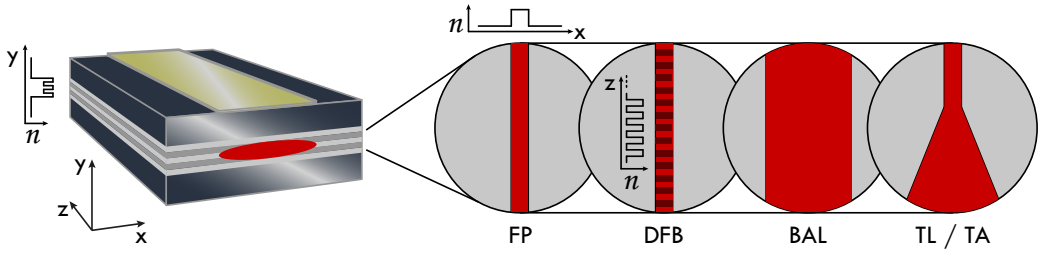

Figure 3.1.: Laser Diode types. On the left a semiconductor chip is depicted (not to scale). The gold layer on top is the metallization for current injection. The architecture of the index of refraction, n, within the active layer forms a waveguide in x and y and determines the emission properties of longitudinal and lateral mode. Tight confinement in x in Fabry-Pérot (FP) and distributed feedback (DFB) diodes results in lateral single mode emission. A grating along z can be implemented to select a distinct longitudinal mode, as in DFB laser diodes. A broad area laser (BAL) has none of this, instead it features a wide active layer for high gain and high output powers. The tapered laser (TL) design enables both, single mode operation and high powers, cf. 3.3 .

Depending on the targeted application a laser needs to meet distinct requirements. Accordingly, during the evolution of laser diodes a variety of different LD types has

come up [23]. For microscopy the smallest possible foci are required, demanding for spatially single mode (SM) lasers. Semiconductor lasers can be manufactured with an implemented waveguide in or close to the active region in order to feature a single mode beam profile, i.e. emission in the TEM_{00} mode [66]. If, on the other hand, the beam profile is less important and high laser powers are needed, LDs with a wide emitting facet, so-called broad area laser (BAL), may be employed (cf. figure 3.1). The laser diodes which emit a TEM_{00} beam can further be distinguished according to their longitudinal mode characteristics, i.e. their bandwidth, $\Delta\lambda$. The simplest SM diode lasers are Fabry-Pérot lasers. Their cleaved facets form the laser cavity, mostly admitting several longitudinal laser modes. To narrow the linewidth of the emission, laser diodes have been developed which include a grating in their active structure. The grating period is much smaller than the cavity length, such that the free spectral range becomes larger than the gain bandwidth and only one lasing mode is allowed. Depending on the exact implementation these lasers are called distributed feedback (DFB) or distributed Bragg reflector (DBR) diode lasers [23].

		BAL	FP	DFB	
CW	P	> 1000	1-500	1-500	mW
	$\Delta\lambda$	> 1	> 1	< 0.001	nm
		mode-locked	Q-switched	gain-switched	
Pulsed	τ_p	< 10	10-80	10-500	ps
	ν_L	> 1000	1-100	1-100	MHz

Table 3.1.: Laser diode characteristics power, P, spectral width $\Delta\lambda$, pulse length τ_p and typical repetition rates ν_L. The pusling parameters are similar for the different laser types, at least in the limits which are given here [68–71].

Independent of the laser type, generally there are three manners of how to operate a laser in pulsed mode: Q-switching, mode-locking and gain switching [30]. In Q-switching the cavity quality factor (Q-factor) is modulated actively or passively. During the low Q-factor phase inversion of the population of states in the gain medium can be established. When the Q-factor is then switched to a high value, stimulated emission sets in due to the cavity feedback and the accumulated population inversion discharges in a single pulse. Mode-locking couples the different longitudinal laser modes with a fixed phase relation. This way, a pulse is synthesized inside the cavity and at each roundtrip some of the light is coupled out of the cavity as a laser pulse. Gain switching, which will be a matter of discussion

in the course of this chapter, relies on a modulation of the pumping, such that the lasing condition is only fulfilled during a short period of time. Semiconductor lasers can be operated in all three modes [67]. Table 3.1 gives an overview of the typical parameters of different LD types in different operational modes.

3.2 Pulsed FP Laser Diodes

Fabry-Pérot laser diodes are among the most popular laser sources which is undoubtedly owed to their properties regarding size, emission control, cost and reliability. This section aims for an analysis of FP LD in an operational mode suited to serve for STED nanoscopy. For this purpose a theoretical fundament for LD dynamics will be presented in 3.2.1, on the base of which simulations were performed as presented in 3.2.2 . The results of these simulations will be considered when the experimental findings of 3.2.3 are interpreted. Furthermore the theoretical and experimental results of this section will provide a background for the discussion of semiconductor amplifiers in the next section.

3.2.1 The Rate Equations of LDs

The two level rate equations were chosen as theoretical approach to describe semiconductor laser emission [72]. It is a phenomenological approach to modeling laser diodes and the most basic theory which is able to treat LD dynamics. Consequently, a number of material properties or physical effects are not taken into account. There are more elaborate theories, up to those giving a full quantum mechanical description of light matter interaction in the material [73–76]. These methods give more insight into spectral and geometric characteristics of the LD emission dynamics. The dynamics of the output power, i.e. the temporal pulse shape, in contrast, are modeled adequately by the rate equation approach [77]. A detailed discussion of the theory of the LD rate equations can be found in the literature [78–80]. The following description was adapted from [81, 82]. In order to analyze semiconductor emission dynamics, the rate equations for the carrier concentration N and the photon number S within the active zone of the semiconductor are considered. The laser diode output power P is directly proportional to S.

$$\frac{dN}{dt} = -g(N)S - \frac{N}{\tau_n} + \frac{\eta_I I}{e \cdot V} \tag{3.1}$$

$$\frac{dS}{dt} = \Gamma g(N)S + \Gamma\beta\frac{N}{\tau_n} - \frac{S}{\tau_c} \tag{3.2}$$

$$P \quad = \quad \frac{V\eta hc}{\Gamma\tau_c\lambda} \cdot S \tag{3.3}$$

The positive contribution in (3.1) is the pumping term, which is given by the injected current $\eta_I I$ normalized by the active volume V and the elementary charge. The gain term $g(N)S$ appears in both rate equations. It describes the interaction of photons with carriers by stimulated emission. Various forms of this term have been discussed [82–84]. In order to take into account nonlinearities at high S the following variant was chosen:

$$g(N)S \rightarrow g_0\,(N - N_0) \cdot \frac{S}{1 + \epsilon S}, \tag{3.4}$$

with the gain coefficient g_0, the transparency carrier density N_0 and the phenomenological gain compression factor ϵ. The other term appearing in both rate equations accounts for spontaneous radiative carrier recombination with the carrier lifetime τ_n. Since only a part of these photons are emitted into the lasing mode, a scaling factor β is introduced in (3.2). In the photon rate equation both, gain and spontaneous emission, are scaled by the optical confinement factor Γ. This factor gives the fraction of the mode energy contained in the waveguide. Finally, (3.2) features a term describing the photon losses due to light outcoupling and internal losses. These are summed up in an effective intra-cavity photon lifetime τ_c. For full parameter reference, refer to table 3.2 .
As already indicated, this theoretical approach makes some assumptions. For example, the gain and current is distributed homogeneously over the whole cavity, neglecting dynamics faster than the cavity round trip time. Furthermore effects attributed to fast carrier dynamics are not considered, which is especially important at high output powers [85]. Similarly, the presented equations do not account for the longitudinal multimode emission of a FP laser diode. Dynamics resulting from interaction between the semiconductor and different laser modes can therefore not be considered [86,87].

3.2.2 LD Simulations

The continuous wave (CW) characteristics of LDs described by equations (3.1) and (3.2) can be found by solving the respective steady state equations numerically for different currents. In order to perform simulations the parameters contained in the rate equations had to be obtained. They were partially taken from literature, while some were chosen such that CW specifications of the simulated device (HL6545MG, Oclaro Inc., San Jose, CA, USA) were obtained from the steady state simulation (see section A.1). The used parameters are summarized in table 3.2 .
In the next step the dynamic response to current pulses injected into the laser

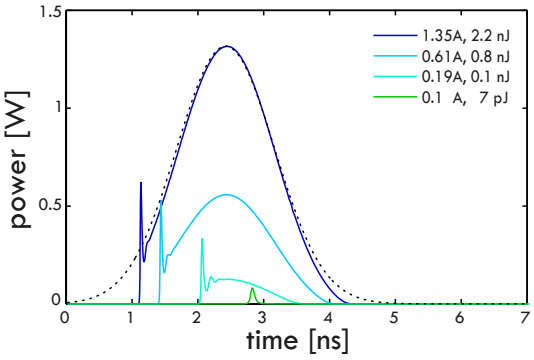

Figure 3.2.: Simulated Pulses of $660nm$ LD. The dotted line is the current ($[a.u.]$) pulse normalized to the largest pulse. Note the close correspondence between the two pulse shapes, the shift in time amounts just to the lifetime of the photons in the cavity. Each laser pulse was generated by a current pulse with maximum current as specified in the legend, where the resulting pulse energies can also be found.

diode was simulated. To this end the rate equations (3.1) and (3.2) were solved numerically for the time intervall of one current pulse. The current pulse was arbitrarily chosen to have a Gaussian shape. Figure 3.2 shows simulated laser pulses generated by injection of these current pulses with different maximum currents. For low currents the characteristic gain switch peak is observed the exact width of which depends on cavity properties. It is, however, much shorter than the current pulse since lasing conditions are only fulfilled for a short time. Up to that time carriers have accumulated in the active volume. The gain switch peak is the sudden discharge of this accumulation. For a direct current (DC) supply signal, the peak would relax in a few oscillations to the steady state output power. In gain switched mode, these oscillations are suppressed by stopping the current pulse, though. For higher peak currents the lasing condition is not only fulfilled during the initial spike, such that longer laser pulses are formed. Increasing the current reveals that the laser pulse shape closely follows the electrical current pulse. Consequently, a laser driver generating current pulses of duration $\tau_I \approx 1ns$ and variable peak currents I_{peak} can operate the diode in two modes with a smooth transition between the two. The FP diodes can then deliver either gain switched laser pulses with a duration $\tau_p \ll \tau_I$ and pulse energies of a few ten pJ if driven at low currents. Current pulses with $I_{peak} \approx 1A$, on the other hand, generate laser pulses with $\tau_p \approx \tau_I$ and pulse energies in the nJ range.

3.2.3 Characterization of Pulsed FP Laser Diodes

The different requirements for excitation and STED lasers in a STED nanoscope have been discussed in section 2.5 . While the excitation laser should feature

Parameters for LD Simulation			
λ	=	$660nm$	wavelength
g_0	=	$1.5 \cdot 10^{-12} m^3 s^{-1}$	gain coefficient
N_0	=	$2.3 \cdot 10^{24} m^{-3}$	transparency carrier density
τ_n	=	$0.9ns$	carrier lifetime
ϵ	=	$8 \cdot 10^{22} m^3$	gain compression factor
V	=	$140\mu m^3$	volume of the active layer
Γ	=	0.4	optical confinement factor
η_I	=	0.9	current injection efficiency
β	=	$4 \cdot 10^{-4}$	radiative coupling coefficient
τ_c	=	$9ps$	intra-cavity photon lifetime
η	=	0.61	extraction efficiency per facet

Table 3.2.: Parameters utilized in the LD simulations. N_0 and η were extracted from a fit to the CW specified values of the laser diode. τ_c was calculated approximately from the cavity properties (see section A.1). All other values were taken from literature [81,82,88].

pulses with $\tau_p \approx 100ps$, the STED laser is required to deliver high pulse energies in ns pulses. The results of the previous subsection suggest that FP laser diodes can be operated to deliver either short and weak pulses or powerful pulses with a longer pulse duration. Fortunately, as a consequence of LD physics and design, the transition happens to occur for pulse durations ranging from ps to ns, which are desirable timescales for STED lasers. This section presents experiments in which LD pulsing characteristics were examined and a maximization of the achieved pulse energy was pursued.

As LD driver an electronic circuitry was developed which generates current pulses of about $2ns$ length. The main component is a high-frequency power metal-oxide-semiconductor field-effect transistor (MOSFET) (D2219UK, Semelab Limited, Lutterworth, UK). It receives a switching signal at its gate, turning on the current. The circuitry contains a network which generates the switching pulses from a trigger signal (e.g. transistor-transistor logic (TTL)). This trigger is able to induce laser pulsing at arbitrary rates ν_L between 0 and $= 50MHz$. A printed circuit board (PCB) was designed for the electronics on which leads were kept short in order to minimize parasite capacities and inductances. For the same purpose the laser diode was soldered directly to this PCB. The peak current could be varied by changing the voltage supplying the main transistor. This way the transition from short pulse mode into strong pulse mode can be achieved. The laser beam was collimated by an aspherical lens. Temporal laser pulse shapes were measured

by coupling this beam to a $20GHz$ photodiode (UltraFast-20-SM, A.L.S. GmbH, Berlin, Germany). The signal was recorded by a $12GHz$ bandwidth sampling oscilloscope (PicoScope 9201A, Pico Technology, St Neots, UK).

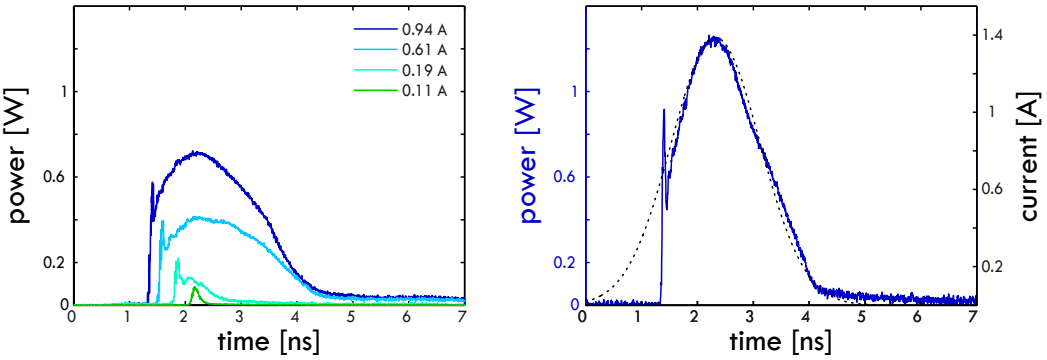

Figure 3.3.: $660nm$ FP LD pulses. Graphic b) shows the highest peak power achieved from this diode type. The pulses shown in a) can be generated on a regular basis. The series illustrates the transition from short gain-switch pulses to strong pulses. From comparison to the simulations (cf. figure 3.2) it can be concluded that the injected current pulse is probably shaped like the dotted curve.

Several laser diodes were tested. The presented results concentrate on what was obtained from a FP laser diode with a central wavelength of $\lambda = 660nm$ (HL6545MG, Oclaro), the parameters of which were also used for the simulations. Due to its high CW output power it promised to be capable of delivering high pulse energies, as required for STED. Nevertheless, the general behavior is similar for all laser diodes. Differences are observed in numbers only, e.g. the exact width of the gain switch peak and possible peak powers. Figure 3.3 a) shows a series of pulses with increasing driving currents. At the lowest current only the gain switch peak forms the laser pulse. At higher currents a second peak emerges, much broader than the gain switch peak. This overdriven peak is first a shoulder to the gain switch peak but finally attains a higher peak power than the latter. Peak powers amount to $P_p = 0.7W$, while the maximum achieved pulse energy in this case was $E_p = 1.5nJ$ with $\tau_p = 2ns$ (FWHM). The current values stated in the legend are approximate values. They were estimated by

$$I_{peak} \approx \frac{\bar{I}}{\tau_p \nu_L}. \tag{3.5}$$

These pulse parameters were obtained reproducibly on a regular basis. A general observation in these experiments was that LD pulses are both, more powerful and

longer if higher currents are applied, while just extending the pulse duration could also be achieved by injecting longer current pulses. In this behavior and also in their approximate output powers the measured pulses agree very well with the simulations.
In order to generate stronger current pulses, thus maximizing the pulse energy, the circuitry was changed slightly and a more flexible trigger signal source was installed. Figure 3.3 b) shows the result of the respective measurement. The maximum peak energy obtained this way was $E_p = 2.3nJ$ with $\tau_p = 1.7ns$. Operating the driver under these circumstances proved to be sensitive to external influence. Additionally such laser pulses could not be reproduced by using an FPGA trigger source, as desired for the STED measurements (cf. 4.1.2). By comparison to the simulations in the preceding subsection it becomes clear, that the peak after the gain switch peak corresponds to the pulse shape of the injected current. Therefore the figure also contains a Gaussian curve depicting the probable underlying current pulse. This current pulse was scaled by distributing the charge per pulse into the gaussian curve.
In summary, pulses from Fabry-Pérot lasers were generated which fulfill the requirements for both, excitation laser and STED laser. This is a main prerequisite for setting up all-semiconductor STED laser systems. The results indicate that more powerful current drivers would enable pulse energies beyond those presented here.

3.3 A Pulsed Tapered Amplifier System

A tapered laser (TL) is a laser diode with a distinct geometry of the active layer, cf. figure 3.1 [89]. It comprises two sections. Similar to a Fabry-Pérot diode the rear section of a TL forms a ridge waveguide (RW). This is followed by the tapered section, the width of which starts at the waveguide width and grows up to the emitting facet of the TL. The emission width is up to 70 times wider than the waveguide [90]. The large width of the active region, as compared to the RW, enables higher gain per length and the wide emitting facet is less prone to catastrophic optical damage (COD), due to lower intensities. At the same time, the taper angle is chosen such that it does not perturb the single lateral mode emerging from the RW section. This way a large fraction of the TL output is concentrated in the fundamental lateral mode, TEM_{00} [91]. Most often, these devices are not used as tapered lasers, but rather as tapered amplifiers (TA), as a special type of semiconductor optical amplifier (SOA) [92–95]. The difference is made by anti-reflection coating of the facets, inhibiting cavity effects. A TA can amplify a so-called seed laser beam, which is coupled into its waveguide, with a gain of over $20dB$ in a single passage, yielding output powers on the Watt level [96].

With the aim of increasing pulse peak powers in semiconductor lasers above the level reached with FP laser diodes, a ns-pulsed all semiconductor MOPA laser system was set up. As power amplifier a tapered amplifier (TA) was utilized which is designed for the amplification of CW light by injecting unmodulated current into the device. The more suitable operational mode for STED is to seed the amplifier with pulses from a gain switched laser diode. In that case there are two options for MOPA operation. First, the amplifier can be driven with a constant current, as specified (pulsed-DC mode). The second possibility is to drive it with a pulsed current, which has to be synchronized with the seed pulses (pulsed-pulsed mode). Finally, pulsing the TA current, a third mode of pulsed operation emerges. If the seed emits CW light but the amplifier is driven with a current pulse, the output signal is determined by the temporal shape of the amplifier current.
This section gives a description and a characterization of the implemented TA laser system. Concerning the chosen parameters, especially the pulse width τ_p, it should be kept in mind that the aim of constructing this laser system was to generate laser pulses tailored for STED nanoscopy. First of all, however, recent work regarding pulsed TA operation shall be reviewed.

3.3.1 Pulsed TA State of the Art

The idea of amplifying not only CW light with TAs has been around for two decades already and several studies, both, theoretical and experimental, have covered the topic [97–100]. In recent years, partially while the work for this thesis was carried out, a number of publications have addressed methods and technologies required for sub-nanosecond pulsed emission from tapered semiconductor devices in more detail. A first approach was to generate picosecond pulses in pulsed-DC mode for second harmonic generation (SHG) [101, 102]. Already then, possibilities of integrating the optical setup were discussed. This idea was pursued in a series of publications about multi-section semiconductor lasers mounted on a microbench [70, 103, 104]. These devices featured an increasing integration of optics and electronics and growing pulse peak powers, up to $65W$. The main motivation for the electro-optical integration was not mere compactness but rather efficient high frequency signal transduction. Consequently this integration enabled the generation of current pulses with peak currents of $I_{peak} = 20A$ and a duration as short as $\tau_I = 2ns$ [105]. The laser pulse properties quoted in these studies amount to widths of $\tau_p = 35ps$ - $120ps$ and pulse energies up to $E_p = 4.2nJ$.
Simultaneously research was carried out to expand the range of possible devices. New taper geometries were proposed and analyzed [106–109]. The possibilities offered by tapered lasers have also gained in importance, especially those devices with a grating in the RW section, as in DFB lasers [75, 110–113].

3.3.2 Laser Set Up

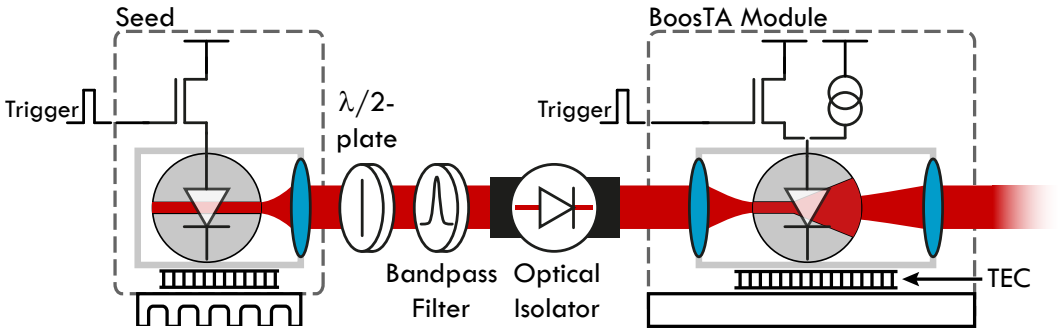

Figure 3.4.: Schematic drawing of the TA system. Both seed laser and TA module are actively temperature controlled by a thermoelectric cooler (TEC). For the case of the seed this control is used to tune the emitting wavelength. The pulsed current supply was not included in the commercial TA module, it is home-built, just as that of the seed diode.

The setup of the tapered amplifier system is schematically depicted in figure 3.4 . The key component is a commercial tapered amplifier module (BoosTA, TOPTICA Photonics AG, Munich, Germany) with a central wavelength of the gain spectrum of $\lambda = 767nm$. It comprises the semicondutor chip itself, active temperature control and DC supply electronics. Furthermore the module houses incoupling optics for the seed, and collimation optics for the output, yielding a slightly elliptical output beam profile. As the source of the seed light a FP laser diode with a central wavelength of $760nm$ (FIDL-30S-760, Frankfurt Laser Company, Friedrichsdorf, Germany) was installed[1]. This diode was driven by gain switch electronics, cf. 3.2. Additionally it was equipped with collimation optics. A thermoelectric cooler (TEC) element was attached to the mounting mechanics in order to tune the emission wavelength of the seed to the amplifier gain maximum by temperature change. An electrical current injected into the TA leads to light emission from both, rear and front facet, the so-called amplified spontaneous emission (ASE)[2]. The emission from the rear facet can act as seed if reflected at the surface of another optical

[1] Two different diodes were employed as seed source. The second is FIDL-30S-770, with $\lambda = 770nm$. Both diodes were tuned to $\lambda = 767nm$ by adjusting the temperature.

[2] ASE is generated by simulated emission, it is not laser emission, though. A spontaneously emitted photon is amplified during propagation through the TA, since it cannot be reflected from cavity mirrors, lasing does not set in.

component. In fact, even the remaining reflection from the collimation optics of the seed diode proved to be sufficient to show this effect. In order to suppress the resulting external self-seeding, two different approaches turned out to be functional. The first and very common approach was to place an optical isolator (OI) (IO-3-780-HP, Thorlabs Inc, Newton, New Jersey, USA) in the seed beam path. This element only transmits light traveling in one direction, while light traveling antiparallely is filtered out of the beam path. It relies on the rotation of the polarization of the transmitted light by different mechanisms [30]. The other method to suppress self-seeding relies on the fact that the emission from the TA is spectrally broader than the seed light. Whereas the latter has a linewidth of about $1.5nm$ (FWHM), the TA ASE spectrum has a width of about $15nm$ (FWHM)(ref). Placing a narrow bandpass filter (LL01-785-12.5, $\Delta\lambda = 3nm$, Semrock Inc., Rochester, NY, USA) between the seed and the TA deflects most of the TA's backward traveling emission out of the seed beam path. Both, seed diode and back traveling TA beam showed an elliptic beam profile. For optimum seed coupling into the amplifier the seed diode was rotated about the beam axis until the long ellipse axes matched. Due to the polarization rotation in the isolator and by beam profile matching the polarization of the seed beam did not match the TA polarization. This can be compensated by placing a $\lambda/2$- plate between seed and amplifier, thus taking into account the polarization dependent amplification.
The output beam of the TA system was coupled into a single mode polarization maintaining fiber. The fiber coupling efficiency η was measured as the ratio of laser powers P_{CW} at the fiber output and in front of the fiber.

$$\eta = \frac{(P_{CW})_{fiber\ out}}{(P_{CW})_{fiber\ in}} \tag{3.6}$$

In CW mode $\eta \approx 50\%$ was reached, indicating proper single mode operation of the TA. In pulsed mode, the ASE is responsible for a large portion of the measured TA power. Since ASE has a multimode beam profile it cannot be fiber coupled efficiently, which makes direct measurement of the fiber coupling efficiency more complicated. Therefore, in pulsed mode an approximate coupling efficiency η_p was considered in order to check the level of fiber coupling.

$$\eta_p = \frac{(\bar{P}_S - \bar{P}_{ASE})_{fiber\ out}}{(\bar{P}_S - \bar{P}_{ASE})_{fiber\ in}}, \tag{3.7}$$

where $\bar{P}_S$ and $\bar{P}_{ASE}$ are the measured average powers with and without injected seed light, respectively. This way only the single mode contribution induced by the seed is included in the coupling efficiency. For some of the measurements which are presented in the next subsections only pulse energies measured at the fiber output are stated. This has two reasons: First, just as for the fiber coupling efficiency,

the pulse energy which is contained within the fundamental lateral mode, and also within the temporal shape of the seed pulse, can be specified more precisely if the ASE contribution is suppressed by fiber coupling. Second, the ultimately important parameter for utilization in STED nanoscopy is the pulse energy carried by a diffraction limited beam, as transmitted by a single mode fiber. Apart from the laser power, and thereby the pulse energy, the temporal shape of the TA output is of particular interest. Measuring the pulse shapes was performed in the same way as described in section 3.2.

3.3.3 Pulsed - DC Operation

The electronics of the seed diode were tuned such that a pulse width of $\tau_p = 1.2ns$ was emitted. The pulse energy of the seed diode behind the filter and the isolator was $E_{seed} = 50pJ$. Amplifier currents of up to the manufacturer specified maximum value of $I_{max} = 2.2A$ were applied. The results are shown in figure 3.5 . It stands out that with increasing currents a growing fraction of the emission is due to ASE. This is because the seed duty cycle is only 0.5% ($\nu_L = 5MHz$) and the lifetime of the pumped carriers is $\tau_n \approx 2ns$ (cf. table 3.2). Therefore, most of the time the TA behaves like in unseeded operation, showing an exponential current characteristic of the ASE. Regarding the measured pulse shapes, one can observe a change with increasing currents. During the first few hundred picoseconds a peak emerges which is not present in the seed pulse. Before the seed pulse arrives carriers have accumulated for about one τ_n. Consequently, the seed experiences a higher gain than the corresponding CW gain at the respective current. After the accumulated carriers have been depleted, the gain relaxes to the CW gain for the rest of the pulse. Apparently, this effect becomes more pronounced with increasing currents. The maximum pulse energy which was obtained behind the fiber was $E_p = 1.2nJ$, after correcting for ASE contributions. Taking into account the fiber coupling efficiency this corresponds to a gain of $16.8dB$ which is above the specified value in CW mode. This can be explained by the described carrier accumulation, while it also indicates proper coupling of the seed into the TA.

At this point there were two motivations to implement pulsing electronics for the TA current. First, low seed duty cycles and high ASE contributions reduce the overall efficiency of the laser and unnecessarily generate background light in the microscopy setup. Moreover, maximizing the laser pulse energy is desirable for STED, as explained in 2.5 . So far, the TA pulse energy at a certain pulse length was limited by the amplifier current, which, in turn, had to be limited to the manufacturer specified I_{peak} to avoid high carrier accumulation levels. For a high DC current such a situation might lead to catastrophic optical damage (COD) at the facets if lasing sets on accidentally. For the case of a ns current pulse, however,

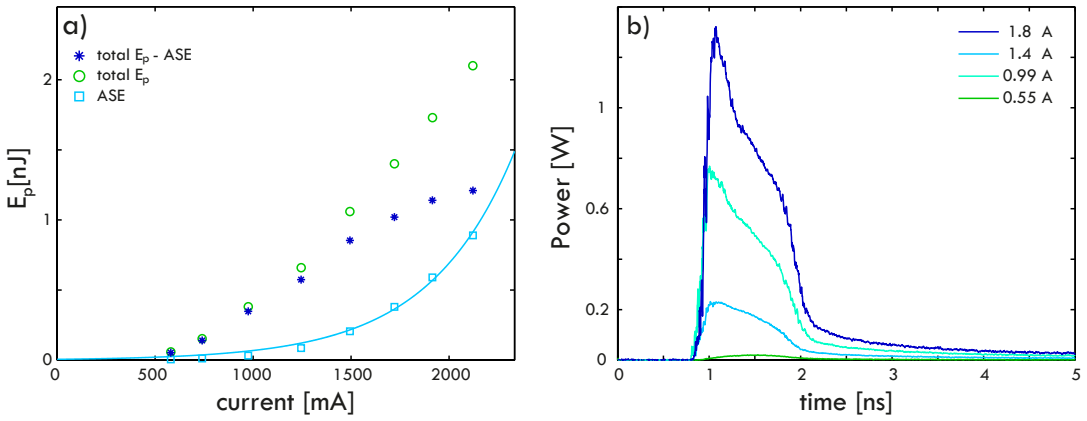

Figure 3.5.: Results of pulsed-DC mode. In a) the current characteristics are depicted. The low seed duty cycle explains the high ASE contribution, following an exponential curve which is fitted by the blue line. The pulse shapes in b) feature a deformation of the original seed pulse. An explanation can be found in the text.

high facet output powers can only last as long as the current pulse. According to the so-called square-root law, the maximum power before COD occurrence scales as $P_{th} \propto \tau_p^{-1/2}$. [114, 115]. That means ns TA pulses can possess substantially higher peak powers than CW emission. Consequently, the TA can be driven at currents well above the manufacturer specified maximum value if ns current pulses are applied.

3.3.4 Pulsed - Pulsed Operation

A circuitry generating nanosecond current pulses was developed. The main switching component is a MOSFET (D1202UK, Semelab), similar to the one used for gain switching of the Fabry-Pérot LD. The Circuit was simulated with a SPICE implementation (Altium Designer, Altium Limited, Sydney, Australia). The simulations indicated that currents of up to $I_{peak} = 8A$ in pulses as short as $\tau_I = 3ns$ could be possible. It should be noted, that for these simulations a proper SPICE model of the TA chip was not available. Also, parasitic properties of the PCB implementation, e.g. lead inductances and capacities, were not taken into account. Therefore, the actually obtained currents were not expected to be as high as in the simulation.
Measuring the pulsed TA current is not a trivial task. This is mainly due to the nonlinear impedance characteristic of the semiconductor chip and the high frequencies involved. A similar method by which the current was determined was

used and described before [105]. It relies on the generation of ASE due to the injected current. For a current pulse, an ASE pulse is obtained, the pulseshape of which can be recorded with the $20GHz$ photodiode, yielding a signal $S(t) \propto P(t)$. Assuming a linear dependence $P_{ASE}(t) \propto I(t)$, with the help of the average current $\bar{I}$, rescaling the measured pulse shape is possible according to[3]

$$I(t) = \bar{I} \cdot \frac{S(t)}{\nu_L \int_0^{1/\nu_L} S(t)dt}. \tag{3.8}$$

Figure 3.6 a) plots the output pulse energy vs. the peak current. The ASE can be fitted by

$$P(I) = P_0 \left(e^{\frac{I}{I_{th}}} - 1 \right), \tag{3.9}$$

corresponding to the output characteristic on an superluminescence diode, which an unseeded TA is [30]. From this it is concluded that the approximation made by $P \propto I$ is adequate to yield proper values for the current. According to this evaluation a maximum current value of $I_{max} = 5.3A$ was reached. As expected, the circuitry cannot generate pulses as high as in the SPICE simulations. The pulse length τ_I increases for increasing I_{peak}, to reach a value of $\tau_I = 6ns$ for the strongest current pulse.
Figure 3.6 shows the TA characteristics in pulsed-pulsed mode. The obtained pulse energies amounted to $E_p = 2.8nJ$ at the fiber output. The corresponding pulse energy at the fiber input is $E_p = 4.8nJ$ with a peak power of $P_{peak} = 7.5W$. The pulse shapes again feature the over-pronounced gain at the beginning of the pulse. For a better understanding of the pulsed amplifier and to get an idea of the value of the TA system for STED nanoscopy, ASE contributions to the signal are considered now.
In figures 3.6 a) and b) the following observations can be made. Although the on-time of the TA current is reduced dramatically as compared to pulsed-DC mode, ASE bears a large portion of the total emission of the laser. For high pulsing currents this is visible in the temporal pulse shapes. The peak of the ASE pulse reaches a level of more than 10% of the actual laser pulse peak. The main pulse induced by the seed, in contrast, does not grow at the same rate, as can also be seen in figure 3.6 a), where the difference of the totally emitted pulse energy and ASE pulse energy is depicted. Whereas the ASE increases exponentially with TA current, the amplifier gain seems to increase proportionally with the current. This suggests that the carriers provided by the pumping current are depleted by photons which are spontaneously emitted in the TA itself, rather than by seed photons.

[3] If $\bar{I}$ is substituted by the average power $\bar{P}$ the same method can be used to scale the power axis of the measured pulse shapes, as is done throughout this thesis.

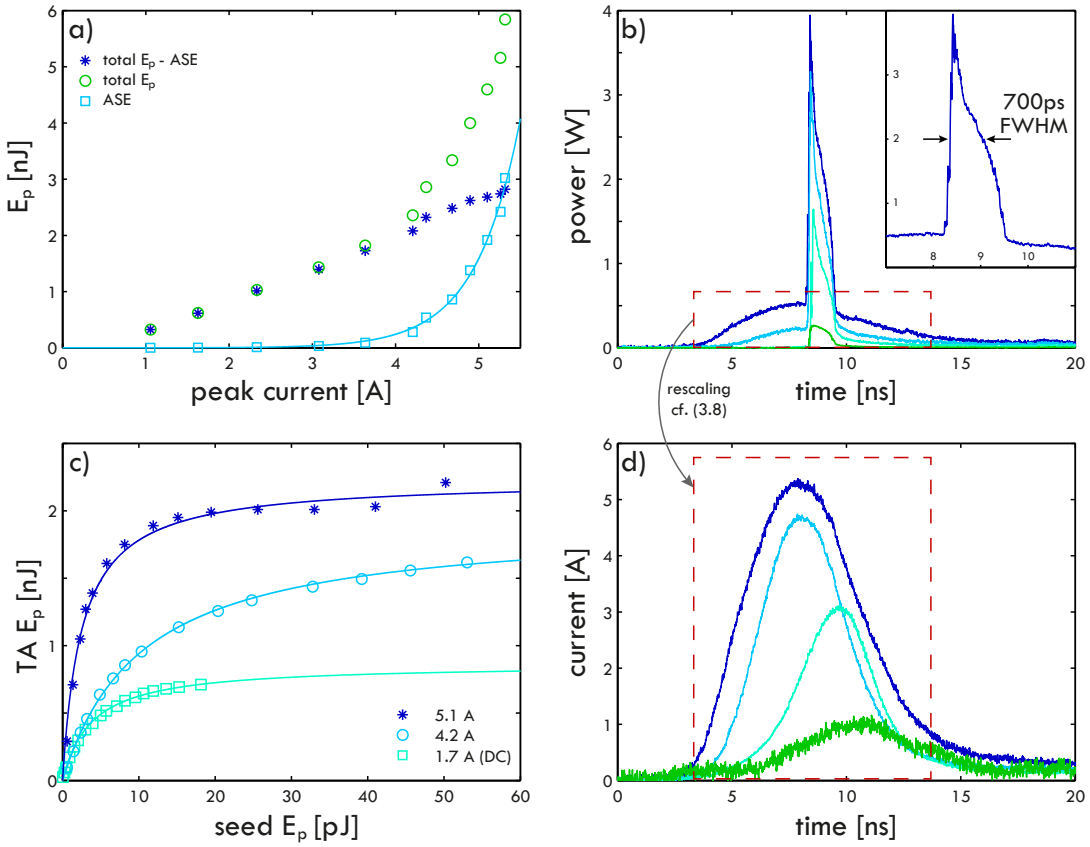

Figure 3.6.: Results of the TA in pulsed-pulsed mode. The measurements of output power and pulse shapes where performed in the same way as for the pulsed-DC mode, results are shown in a) and b). The peak currents of the current pulses were calculated with the help of the ASE pulse and d). In c) the dependence of the TA output on the seed power for different currents is depicted. Notably, the highest current requires the least seed input to reach saturation.

This conclusion is supported by yet another observation. The $\lambda/2$-plate in the seed beam path can be used to tune the seed power. Measuring the TA output power in dependence of the seed power yields a saturation curve as shown in figure 3.6 c). This behavior is observed in both, CW and pulsed mode. Saturation curves of the type

$$E_p(E_{seed}) = E_0 \frac{E_{seed}}{E_{1/2} + E_{seed}} \tag{3.10}$$

were fitted to the measured data to determine the saturation parameter $E_{1/2}$. First the seed power required to saturate amplification increases with increasing TA cur-

rent, since more carriers are available for stimulated emission. This behavior is not observed when going to higher pulsed currents, as is shown in figure 3.6 c). On the contrary, the highest TA current requires the least seed power for saturation. As indicated, a possible explanation is the competition for stimulation of emission between photons of seed and ASE, respectively. In the following this phenomenon is referred to as seed competition.

3.3.5 CW - Pulsed Operation

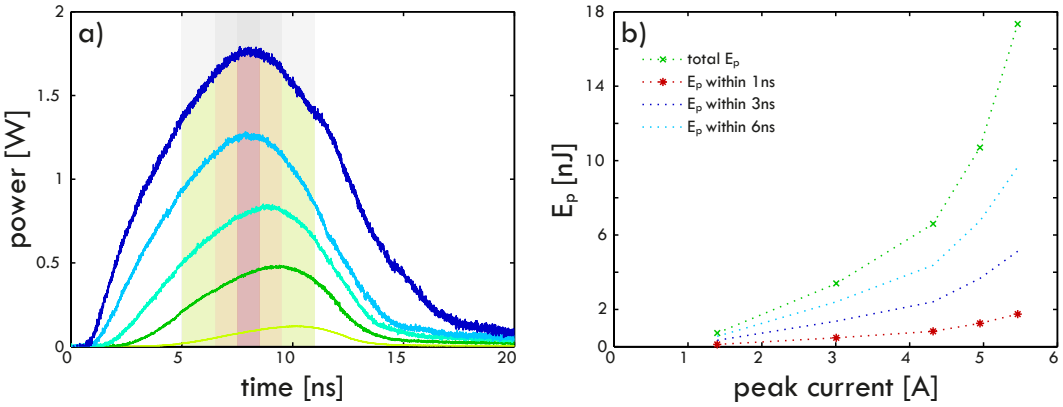

Figure 3.7.: Results in CW-pulsed mode. Although peak powers do not exceed $2W$, $E_p = 17.3nJ$ could be obtained. The distribution of this energy into intervals of $1ns$, $2ns$ and $6ns$ around the peak is shown in b), while the shaded regions in a) mark the respective areas for the case of the strongest pulse.

The third possibility to obtain pulsed laser emission from the TA system is to utilize a CW seed which is amplified by a pulsing TA. Due to the fact that the TA current pulses are longer than those of the gain switching electronics, the laser pulses are expected to be longer in this mode than in the other two. Pulses and their respective pulse energies are shown in figure 3.7 . As expected the pulse lengths of $\tau_p = 5.5ns$ - $10ns$ are considerably longer than for a pulsed seed. Additionally, it is remarkable that the pulses are significantly longer than the ASE pulses (cf. figure 3.6 d)). This is due to the exponential current characteristic of ASE emission. Currents at which ASE is still negligible suffice to provide amplification of seed light. The peak powers reached in CW-pulsed mode are not as high as in pulsed-pulsed mode, since there is no initial stimulated emission burst, as was the case for pulsed seed light. Nevertheless the long pulse duration enables pulse energies of up to $E_p = 17.3nJ$ and $E_p = 28.2nJ$ behind the fiber and in front of it, respectively. For application in STED, only the pulse energy emitted within

one fluorophore lifetime τ_s is useful. The energy contained within time intervals of different lengths around the peak is plotted in figure 3.7 b). It becomes clear that if an organic dye is addressed, with $\tau_s \approx 3ns$, only a part of the energy of such pulses can be used. If, on the other hand, fluorophores with a longer fluorescence lifetime were used, the CW-pulsed mode may become attractive. Such a case will be presented in section 4.4 of the next chapter.

3.3.6 Two-Contacts TA

To further investigate the seed competition, a single tapered amplifier chip was acquired (EYP-TPA-0765-02000-4006-CMT14-0000, Eagleyard Photonics GmbH, Berlin, Germany). It possesses separate electrical contacts for the RW section and the tapered section. Mechanics and optics which showed the same functionality as the commercial module were designed and fabricated in house. The mount for the seed diode was integrated in the mounting mechanics. An electrical circuitry providing current pulses for RW section and taper section separately was designed. In the design of both, mechanics and PCB, care was taken of keeping leads to the TA as short as possible, minimizing parasitic effects (see figure A.3).
First The output power of this two-contacts (TC) TA system was measured in pulsed-pulsed mode, i.e. both TA sections received current pulses. The obtained current pulses were shorter than $\tau_I = 3ns$ with a peak current of $I_{peak} = 5A$. This was evaluated from the ASE trace in figure 3.8 a). The same figure shows pulses obtained by pulse seeding. They are considerably shorter than those obtained from the single contact TA. This is attributed to the short current pulse, which does not supply carriers for amplification of the trailing edge of the seed pulse.
Since the RW section was expected to have some influence on seed competition, the supply voltage for the current through this section was varied. The results are shown in figure 3.8 b). Increasing the RW Voltage, thus the RW current, yields higher total output powers, which are sown as dashed lines. The seed induced contribution, however, does not grow in the same manner, at least not in pulsed-pulsed mode. The energy carried by the seed induced pulse decays starting at a certain RW current, which is reached earlier for higher taper currents. Operated in CW-pulsed mode the TA shows a different behavior. In this case the two TA sections are still pulsed, but a CW seed is utilized. Applying higher RW current in this mode, not only yields higher ASE but also higher pulse energies after subtraction of the ASE. Additionally the short current pulses delivered to the two-contacts TA enable short pulsing in CW-pulsed mode as well. A pulse width of $\tau_p = 1.8ns$ was obtained with a peak power of $P_{peak} = 4.4W$ in front of the fiber.
In total the fiber coupled pulse energy which was reached with the two-contacts TA did not exceed the pulse energy obtained from the single-contact pulsed TA. This is

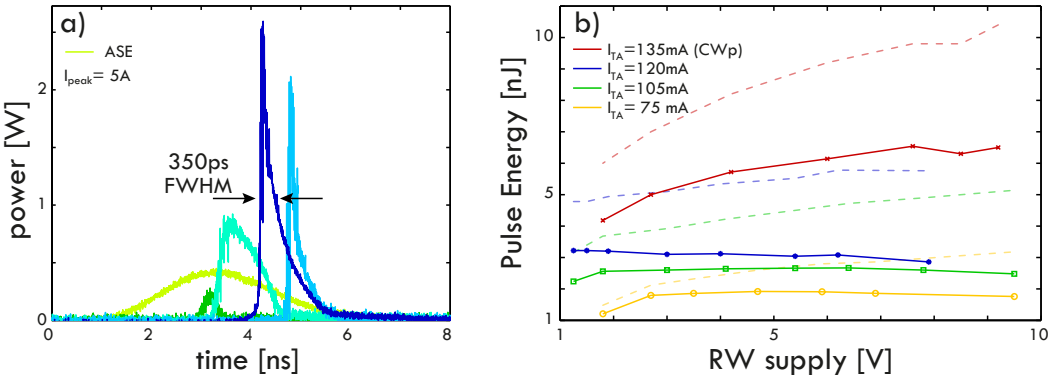

Figure 3.8.: Results from the two-contacts tapered amplifier. a) Temporal pulse shapes with variation of the trigger time of the seed. Due to the short ASE pulse the seed pulse is only amplified to its full length when it arrives early, such that the carrier burst can not yet be exploited (turquoise trace). For a seed arriving later the trailing edge (blue trace) or even the whole pulse (light blue trace) cannot be amplified with a high current level. The wide shape is the ASE pulse, the y-axis of which is not scaled. b) Seed competition by RW section in CW-pulsed mode (red) and pulsed-pulsed mode. The dashed lines include ASE while the solid lines do not. In pulsed-pulsed mode a RW current exists at which a maximum seed induced E_p is obtained. In CW-pulsed mode the seed induced E_p keeps increasing with increasing RW current.

partially attributed to the short current pulses through the tapered section. Peak powers reached in pulsed-pulsed mode were similar for the two devices. Therefore STED nanoscopy was performed with the single-contact TA system. The pulse energies which were achieved are expected to result considerable resolution enhancements. Thus, the aim of providing higher pulse energies from semiconductor lasers was reached with the tapered amplifier approach.

3.4 A Green ps-Pulse Semiconductor Laser Module

The challenge which semiconductor laser development is currently facing is the wavelength gap in the green-yellow range. Wavelengths between $525nm$ and $625nm$ are so far being accessed by e.g. diode pumped solid state (DPSS) lasers [116]. They are convenient due to their compact size and reliability. The dynamics of the laser states in the solids inhibit pulsing on the ns scale, though [117]. Another way to access this wavelength range is frequency doubling, more generally, frequency conversion. The nonlinear processes which are involved in these schemes require high laser intensities in the interaction volume of the fundamental light and the nonlinear medium. Therefore, such lasers often feature a multi-stage

amplifier design [118, 119], or the conversion efficiency is increased by passing the nonlinear medium multiple times [120]. Instead of generating high powers and focusing it to high intensities over a short range, another approach is to confine the fundamental light within a waveguide. This method can make profit of both, the high intensity within the waveguide and a long interaction range, given by the waveguide length [121–123].

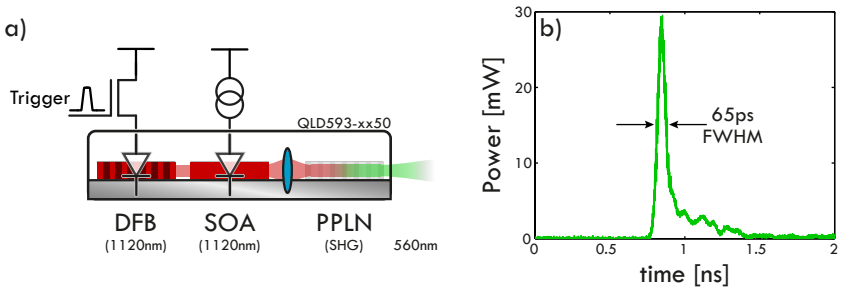

Figure 3.9.: Scheme of a green-yellow *ps* pulsed semiconductor laser source. The working principle of the laser module is depicted in a). The commercial laser module comprises a narrow linewidth distributed feedback (DFB) laser diode and a semiconducto optical amplifier (SOA) which are monolithically integrated. The SOA output is focused into a nonlinear crytal (PPLN) in waveguide structure. An exemplary $560nm$ pulse is shown in b), with $E_p = 4pJ$.

Recently a laser module has become commercially available featuring a monolithically integrated semiconductor MOPA system and a frequency doubling periodically poled $LiNbO_3$ (PPLN) crystal in waveguide structure (QLD0593-xx50, QD Laser Inc, Kawasaki, Japan). It is available at converted wavelenghts of $532nm$, $561nm$ and $594nm$, bridging the GY-gap completely. Since amplification and frequency doubling are performed during a single pass through the respective device, the dynamics of the emission is directly determined by the laser diode. In addition to CW operation, this enables fast modulation of the green emission, in particular frequency doubling of gain switch pulses.
In order to generate such pulses a module with $\lambda = 561nm$ was equipped with suitable electronics. While the DFB diode, i.e. the master oscillator (MO), was driven by the well proven gain-switch electronics, the semiconductor optical amplifier as power amplifier (PA) was DC supplied, which produced ASE at the fundamental wavelength of $1122nm$. Due to the nonlinear frequency doubling the green emission due to ASE, with a peak power in the nW range, was negligible. Pulses with $\tau_p \approx 100ps$ and $E_p = 4pJ$ were obtained from this device, cf. figure 3.9. Repetition rates of $\nu_L = 100MHz$ were possible. The pulse depicted in figure 3.9

b) was measured to have $\tau_p = 65ps$. Since this is already close to the minimum pulse width which can be recorded with a $12GHz$ sampling oscilloscope, the actual pulse length might even be shorter. Another laser of this type was set up with $\lambda = 594nm$ showing similar performance (see figure A.2). The obtained pulse parameters make these laser modules ideally suited as excitation laser sources in fluorescence imaging applications in general and STED nanoscopy in particular.

Semiconductor Lasers in STED Nanoscopy

4

In the preceding chapters the foundations were laid for the construction of a STED nanoscope with a laser system consisting purely of semiconductor lasers. Both, in technical and in practical regard such a laser system features big advantages over STED laser systems which were so far available. In particular, chapter 3 presented semiconductor lasers which were tailored for the use in STED nanoscopy. For the purpose of testing the performance of these lasers a STED nanoscope was set up in easySTED arrangement.
Since two STED laser systems were developed at different wavelengths, two such setups were necessary. The similarities in these setups were exploited such that a single machine was set up which could accommodate both wavelength modes. The parts which were necessarily different were arranged in the same architecture. Only the laser systems of the two resulting nanoscopes differ notably from each other. Accordingly, the first section of this chapter describes the nanoscope excluding the laser systems. These are described in 4.2 and 4.3 and so are the results which were obtained with each system.
The properties of the TA STED laser system enabled access to a new application of STED. For the first time it was possible to perform STED imaging on so-called fluorescent nuclear track detectors. Section 4.4 presents these results.

4.1 easySTED Nanoscopy Setup

4.1.1 Optical Setup

Figure 4.1 is a schematic drawing of the optical setup for the two-color-modes nanoscope. A polarization maintaining fiber (PMF) is utilized as common light source of excitation and STED laser, such that the two wavelengths are available as perfectly aligned single mode Gaussian beam. Except for alignment mirrors, the only element between the collimation lens and the scan lens is the filter which separates the beam paths of illumination and fluorescence. In order to minimize the effect of the filter onto the laser beam wavefront, a filter was chosen which can be used in transmission for both, excitation laser and STED laser. These filters, which are different ones for each color mode, are specified in the repsective laser subsection. A beam scanner in QUAD scanner design is utilized [44], the housing

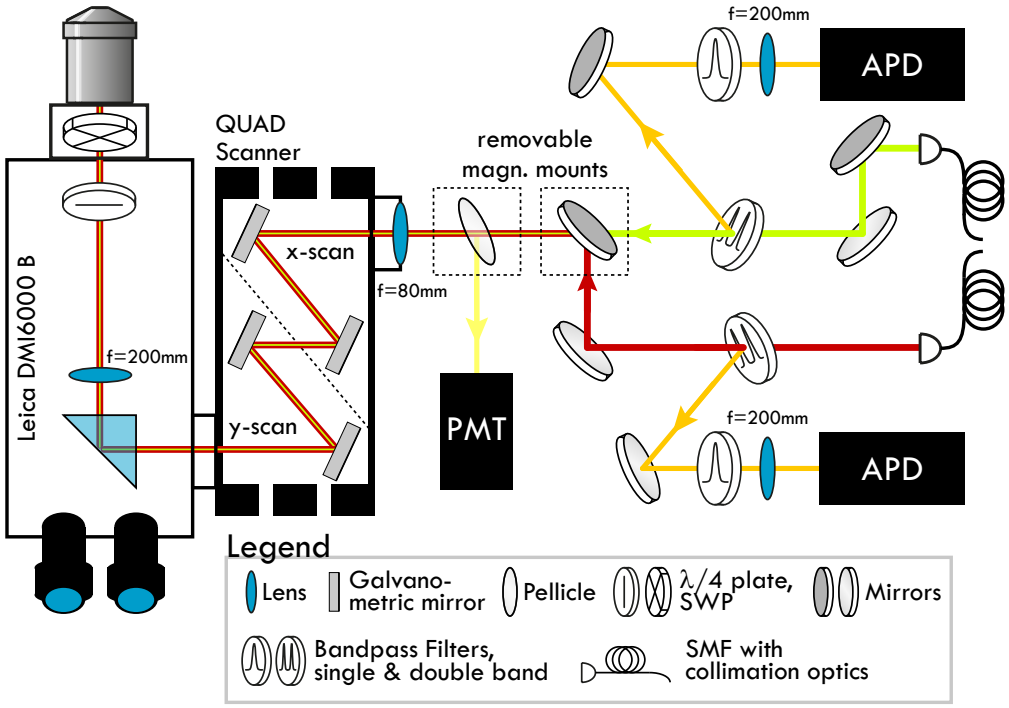

Figure 4.1.: Optical setup for the two-color-modes easySTED nanoscope. The lasers are delivered by single mode fiber. If the magnetic mirror mount is removed, instead of the red illumination path (corresponding to the red-infrared laser system) the green illumination can be applied (green-red laser system) and the respective detection will be utilized. All optical elements of the setup are shown.

of which is attached to a microscope stand (Leica DMI6000 B, Leica Microsystems, Wetzlar, Germany). This stand provides the tube lens and an objective revolver. If required, it also gives the possibility of Hg lamp illumination and sample overview through eye pieces. The scan lens focal length was chosen such that in combination with the tube lens the illumination beam is stretched to fill the back aperture of the objective lens. The easySTED waveplate is mounted right below the objective lens. The employed objective lens is a Leica $NA = 1.4$ oil immersion objective. The fluorescence beam is separated from the illumination as mentioned and then passes two identical band-pass filters to block residual reflections of laser light (FF01-605/64-25 for the green-red setup, FF01-697/75-25-D for the red-IR setup, both Semrock). Subsequently the fluorescence is focused onto an avalanche photodiode (APD) used in photon counting mode (PDM 100, Micro Photon Devices, Bolzano, Italy for the green-red setup; SPCM-AQR, PerkinElmer Optoelectronics GmbH, Wiesbaden, Germany for the red-IR setup). The APD chip was utilized as confocal

detection pinhole. For this purpose the focal length of the focusing lens was chosen such that it generates a focus of the size of the APD active area. An optional detection beam path for non-confocal detection by a photo multiplier tube (PMT) can be introduced by placing a pellicle beam splitter on a magnetical optics mount right in front of the scanner. Everything in the described setup from the scanner to the objective lens, and the PMT beam path, is shared by the beam paths for the two color modes. A removable mirror placed on another magnetical optics mount is utilized to switch between the different color modes.

4.1.2 Electronic Control & Data Acquisition

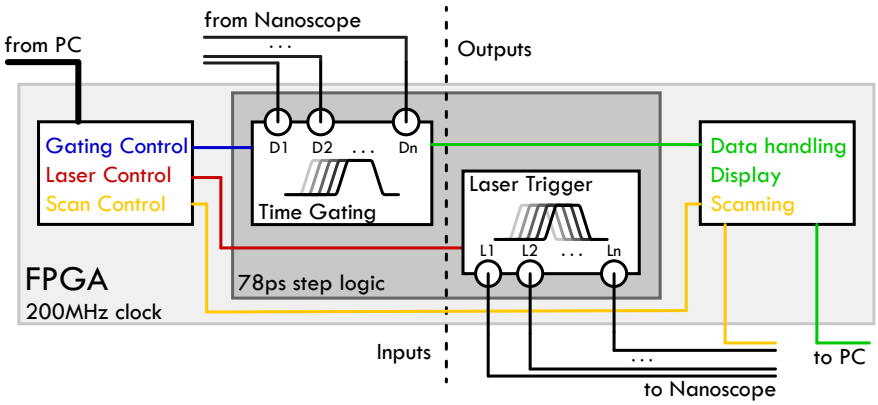

Figure 4.2.: Nanoscope control via FPGA. Processing of the incoming signals and laser trigger generation is implemented with a timing logic which allows for time steps of $\approx 78ps$. All other signals are handled with a $200MHz$ clock.

Microscope control and data acquisition is performed by one single FPGA board in a PC (NI PCIe-7852R, National Instruments GmbH, Munich, Germany). The nanoscope control software is home-built and has been used in a similar version in other experiments [44]. Its most important tasks are scanner control, laser triggering and data acquisition, processing and display. Data processing refers mainly to time gating. In order to perform time gated STED the FPGA evaluates the signal collected by the APD with a time step size of $5ns/2^6 \approx 78ps$.
The same timing logic is employed for the outputs for laser triggering, such that optimization of laser synchronization is adjusted in the software. The individual control of every laser trigger pulse further enables the generation of laser pulses on demand, e.g. for line multiplexing, pulse multiplexing or interleaving of various pulse modes. Apart from shifting the trigger pulse in total, also the trigger pulse length can be varied, which finds application in the TA current pulse generation. The combination of this laser control with semiconductor lasers results in a flexi-

bility which is unique in STED nanoscopy. It is benefitial e.g. to adapt the laser conditions to the requirements of a certain sample, as in the example presented in section 4.4 .
The other signals which have to be processed by the FPGA board are handled with the standard $200MHz$ clock timing. No higher precision is required in those cases, since the relevant time scales for scanning and display are μs to ms.

4.2 Green - Red LD STED System

4.2.1 Laser System

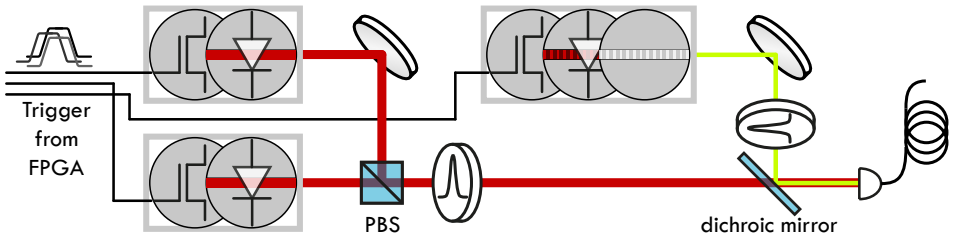

Figure 4.3.: $560nm$ - $660nm$ LD STED laser system. Two of the Fabry-Pérot laser diodes at $660nm$, examined in 3.2, together with the module described in 3.4 form a laser diode STED laser system. The red laser diodes are arranged such, that their beams can be combined by a polarizing beam-splitter with negligible loss. The bandpass filters can be utilized for tuning the laser power.

The $560nm$ - $660nm$ LD STED laser system was designed around LDs as STED lasers. A sketch of the laser system is shown on figure 4.3. An easySTED waveplate for $660nm$ was manufactured by B. Halle Nachfl. GmbH, Berlin, Germany. This phaseplate shows near to perfect constructive interference at $560nm$, so this wavelength was chosen for excitation. The gain switched frequency doubled laser module described in section 3.4 is the designated excitation light source. After collimation it is cleaned up spectrally by a narrow band-pass filter (LL02-561-12.5, Semrock). The excitation power is tuned by tilting this filter.
The STED laser comprises two $660nm$ LD as described in section 3.2. The two diodes were oriented such that their polarizations are crossed, thus they can be merged by a polarizing beam splitter (PBS). The merged STED laser beams are also cleaned up spectrally (LL01-671, Semrock) and merged with the excitation beam through a dichroic mirror (Di02-R635-25x36, Semrock). The three coaligned beams are coupled into a PMF. A fiber coupling efficiency of up to 65% and 55% were obtained for the STED laser and the excitation laser, respectively. As mentioned above, in the microscopy setup a multi-band-pass filter is employed for the

separation of illumination and fluorescence. In the case of the green-red system this filter is of the type FF01-515/588/700-25 (Semrock). At an inclination of 25° to 30° relative to the illumination beam this yields a reflected detection band of about $40nm$ width, while the transmission of both lasers is above 90%.

4.2.2 Results

The wavelength combination of the LD STED system is ideally suited for the use with the dye ATTO565. Before turning to biological samples stained with this dye, however, the performance of the system was tested with technical samples. Polystyrol beads filled with organic dyes are popular technical samples. Two types of these were used with LD STED, nile red fluorescent FluoSpheres and red fluorescent FluoSpheres (Fisher Scientific GmbH, Schwerte, Germany) with absorption and emission peaks at ($535nm/575nm$) and ($580nm/605nm$), respectively. Figure

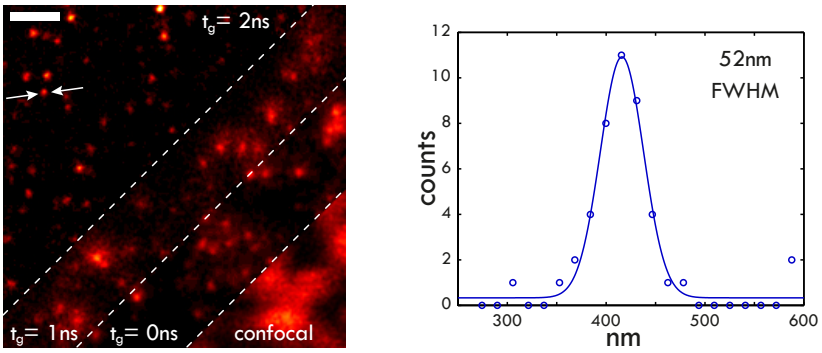

Figure 4.4.: LD STED imaging of nile red fluorescent beads, smoothed raw data. Parts of the image are depicted with different gating settings. The diffraction limited signal contributing to the image for early gate starting times t_g can be observed. The graph shows a profile of the bead marked with arrows and a Gaussian fit to extract the FWHM. Scale bar is $500nm$.

4.4 shows an image taken of a sample of $20nm$ sized nile red fluorescent beads, diluted 1 : 40.000. Recording conditions were

$$E_p^{ex} = 2.5pJ \quad E_p^{STED} = 0.9nJ \quad \nu_L = 10MHz \quad \mathrm{t}_{px} = 116\mu s,$$

where t_{px} is the pixel dwell time and pulse energies are values in the focus. Furthermore a threefold line accumulation was used to receive more photons. The direct triggering of the semiconductor lasers makes line multiplexing of STED and confocal mode possible. Thus the images are virtually acquired simultaneously. The APD signal generated during STED imaging is evaluated by three channels, each

with different time gating settings. The resulting imaging qualities are visualized in different parts of the image in figure 4.4. This demonstrates the effect of time gated detection in combination with relatively long STED pulses. The ungated signal comes with a significant diffraction limited blur around the highly resolved spots. Only if the gate staring point is chosen to be $t_g = \tau_p = 2ns$ this blur is eliminated. With these settings the beads could be imaged with a resolution of $\Delta x \approx 50nm$ as is demonstrated by fitting a Gaussian curve to a line profile of one bead.
A sample of PTK cells in which vimentin was antibody labeled with ATTO565 (ATTO-TEC GmbH, Siegen, Germany) was examined to demonstrate the imaging capability of the LD STED system in biological samples. Imaging was performed under almost identical conditions as for the beads. Since the fluorophores tend to have shorter lifetimes in a biological environment, the STED laser was shifted slightly in time, so was the gate starting time. Furthermore, the excitation pulse energy was tuned to $E_p^{ex} = 1.2pJ$ because the sample was labeled so densely as to lead to saturation of the APD at stronger excitation. Figure 4.5 shows the results of such a recording. The resolution obtained at single antibodies was between $60nm$ and $70nm$.

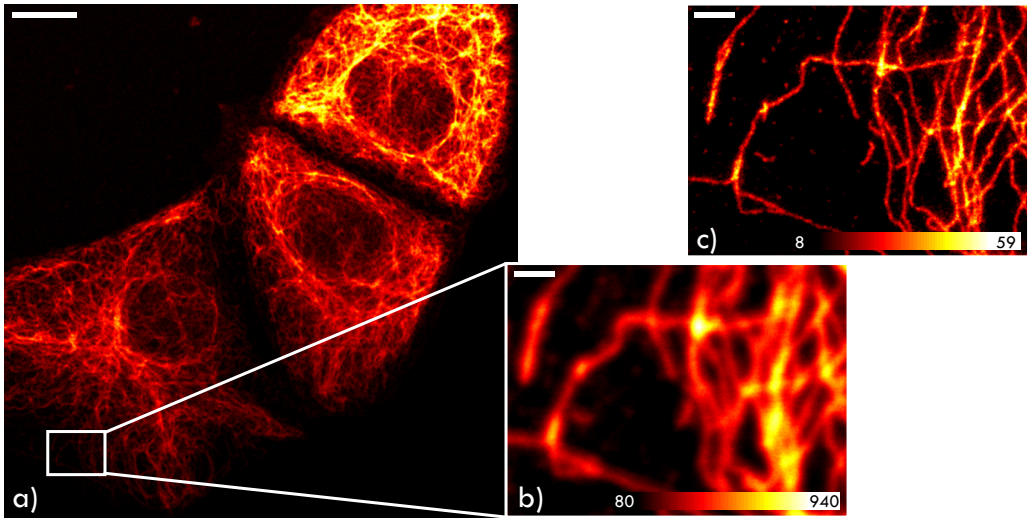

Figure 4.5.: LD STED imaging of a biological sample, smoothed raw data. Vimentin in PTK cells was stained with ATTO565. In b) and c) the white bordered region of a) is shown in confocal and STED imaging mode, respectively. Scale bars are $10\mu m$ in a) and $1\mu m$ in b) and c).

4.3 Red - IR TA STED System

4.3.1 Laser System

The second all-semiconductor STED laser system which was set up in the course of this thesis comprises the pulsed tapered amplifier laser system presented in 3.3 as STED laser, and a pulsed FP diode as excitation laser. This TA STED laser system is depicted in figure 4.6 . The corresponding easySTED segmented waveplate was manufactured by B. Halle Nachfl. GmbH for a wavelength of $\lambda_{STED} = 767nm$, which is the gain maximum of the TA. The excitation laser has a wavelength of $\lambda_{ex} = 640nm$ (HL6385DG, Oclaro Inc.), which yields close to perfect constructive interference after passing the SWP. The excitation laser is cleaned up by a narrow band-pass (LD01-640/8-12.5). The two lasers are merged by a long-pass filter (BLP01-785R, Semrock), which also serves to block the low wavelength tail of the TA ASE spectrum. This light might otherwise be visible in the detection band. Both beams are coupled into a PMF to be guided to the microscopy setup. The beam splitting filter for this laser combination is the multi-band-pass filter FF01-650/780/880 (Semrock), which generates a detection band between $645nm$ and $760nm$ at an inclination of 19° relative to the laser path. More than 90% of the laser power is transmitted in this arrangement.

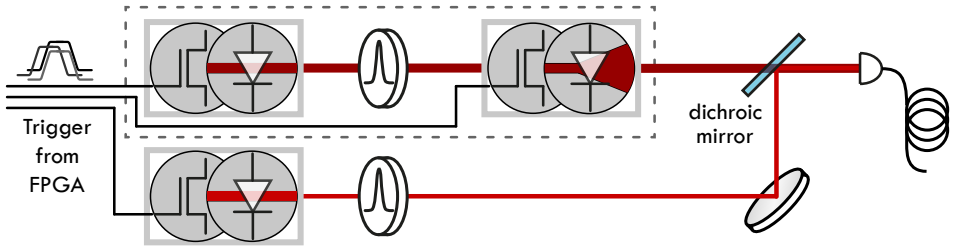

Figure 4.6.: $640nm$-$767nm$ TA STED laser system. The pulsed TA system as described in 3.3 (dashed box) was complemented with a gain-switched Fabry-Pérot laser diode at 642nm as excitation laser, which is cleaned up by a narrow bandpass filter. They form a STED laser system which can target popular infrared emitting dyes.

4.3.2 Results

Like the LD STED system, the TA STED system was first tested with fluorescent beads. Spectrally suitable beads are Crimson FluoSpheres ($625nm/645nm$) and dark red FluoSpheres ($660nm/680nm$)(both Fisher Scientific GmbH, Schwerte, Germany). Figure 4.7 a) shows a STED image of a sample of $20nm$ sized Crimson

beads. The parameters of the TA STED system were

$$E_p^{ex} = 2pJ \quad E_p^{STED} = 1.1nJ \quad \nu_L = 5MHz \quad \mathrm{t}_{px} = 100\mu s \quad t_g = 1.4ns,$$

and a threefold line accumulation was used. The resolution reached with these

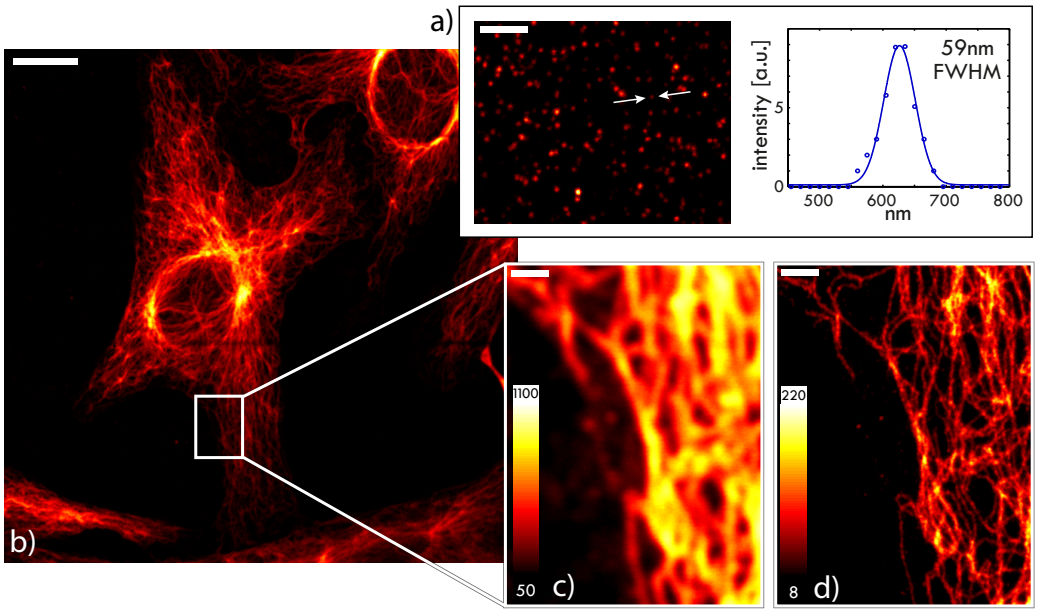

Figure 4.7.: Results of TA STED nanoscopy, smoothed raw data. a) $20nm$ Fluorescent Crimson beads and Gaussian fit of a bead profile, scale bar $1\mu m$. b) Confocal image of Vero cells with STAR635P labeling of Vimentin, scale bar $10\mu m$. For the recordings of c) and d) the region of b) marked with a white border was simultaneously imaged in confocal and STED mode by line multiplexing. Scale bars are $1\mu m$.

settings was $\Delta x \approx 60nm$. Time gated detection was utilized for the measurement, reducing the diffraction limited background. Due to the shorter pulses of the tapered amplifier, at optimum resolution the gate delay t_g could be chosen shorter than in the case of the LD STED system, which improves the effective detection efficiency.
The TA STED nanoscope was also tested with biological samples, the results of which are shown in figure 4.7 b) - d). Vimentin was labeled in Vero cells with antibody conjugated STAR635P (Abberior GmbH, Göttingen, Germany). In order to avoid saturation of the APD signal due to the high labeling density the excitation laser was attenuated to $E_p = 1.2pJ$ for these measurements.
The measurements presented so far already demonstrate the high potential of semiconductor lasers for STED imaging. In addition to the data presented so far,

an exclusive application for the TA STED system was found. STED imaging of fluorescent nuclear track detectors was successfully performed for the first time, which is presented in the next section.

4.4 FNTD STED Imaging

In biological applications the most commonly used fluorophores are organic dyes and fluorescent proteins [31]. These feature fluorescence lifetimes of about $\tau_s = 3ns$, setting the timescale for possible STED action. Apart from these systems there is another fluorophore which has been utilized successfully in STED nanoscopy, namely nitrogen vacancy color centers in diamonds [26, 124–126]. Of course there is a multitude of other systems, especially in crystalline solids, possessing similar properties as this type of color center [127–130].

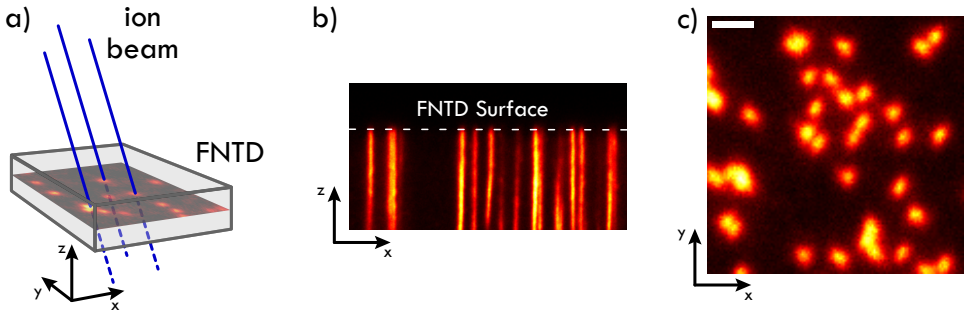

Figure 4.8.: FNTD ion tracks, smoothed raw data. Irradiation of the FNTD with ions is schematically depicted in a). Along z the ion tracks appear as fluorescent stripes as shown in b). c) shows a confocal image of the x-y plane of an FNTD, scale bar is $1\mu m$.

One of them has actually found application with fuorescence microscopy. So-called fluorescent nuclear track detectors (FNTDs) consist of a Al_2O_3 single crystal with Carbon and Magnesium doping. The doping creates color centers which are aggregate defects formed by two oxygen vacancies and two Mg^{2+} impurities. By capturing a secondary electron originating from high energetic particle irradiation such a color center be activated into a state which shows absorption around $620nm$ and emission around $750nm$, with a fluorescence lifetime of $\tau_s \approx 75ns$ [131]. These states are long-lived and can be read out by fluorescence microscopy, e.g. visualizing the path an ion took through the crystal as illustrated in figure 4.8. Due to this possibility FNTDs are used for radiation field monitoring and to examine ion irradiation of biological tissue, which is comparable to radio therapy of cancer.

The aim is to correlate irradiation induced damage in the samples to the radiation dose [132, 133]. For this purpose the width of so-called track spots in the crystal can be measured. A track spot is a fluorescently activated area around the location of ion penetration. The size of this area, where secondary energy transfer processes have activated color centers, depends on the linear energy transfer of the ion. This has been demonstrated for heavy ions which generate track spots of a few micrometers' width [134]. The clinically relevant ions H^+ and C^{6+}, however, leave track spots too small to resolve by conventional microscopy.

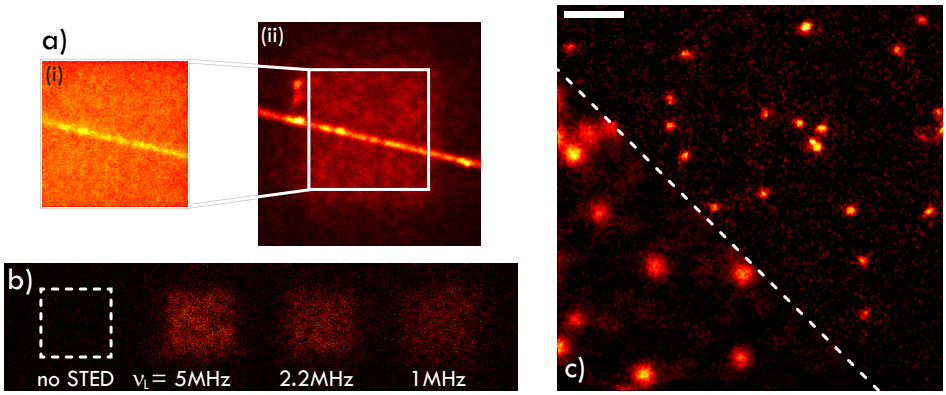

Figure 4.9.: STED imaging of ion tracks in an FNTD, smoothed raw data. a) Ion trace in the FNTD imaged with STED (i). A high background is observed which is due to activation of the color centers due to STED beam irradiation. This is proven by zooming out and taking a confocal image of the region (ii). b) Repetition rate dependence of FNTD activation by the STED laser at equal photon doses. $\nu_L = 1MHz$ is chosen for subsequent recordings. c) Confocal and STED image of FNTD proton track spots with a STED pulse energy of $E_p = 3.9nJ$ in the focus. At irradiations the protons had an energy of $49MeV$. The spots could be resolved down to $\Delta x = 110nm$, scale bar is $1\mu m$.

Therefore STED measurements were performed on such samples. The spectral properties make the red-IR TA STED system ideally suited for these studies. An image which was taken under similar conditions as employed for imaging of organic dye samples is shown in figure 4.9 a). It features a high background which inhibits resolution enhancement. The figure also shows the same region in a confocal recording revealing a permanent fluorescence activation in the region where STED imaging was performed. This is attributed to the fact that the color centers are not only sensitive to ionic radiation, but they can also be activated by UV light [130]. The activation might therefore stem from sequential multi-photon processes or excited state absorption. The probability of the latter increases if the

ratio of fluorescence lifetime and laser repetition rate decreases. A dependence of the activation by STED on the pulse frequency ν_L is demonstrated in figure 4.9 b). At equal photon doses the FNTD shows more activation by the STED beam if higher repetition rates, ν_L are used. Due this $\nu_L = 1MHz$ was chosen for further FNTD STED imaging. The necessity of this relatively low repetition rate is partially attributed to the long fluorescence lifetime of the color centers. On the other hand this long τ_s also enables utilization of a STED laser pulse of longer duration, as available from the TA system in CW-pulsed mode. Pulse energies up to $E_p = 10nJ$ are utilized, while at the same time the applied laser peak power is relatively low, which is beneficial with respect to undesired multi-photon processes. Figure 4.9 c) shows results of FNTD STED recordings which were taken with a repetition rate of $\nu_L = 1MHz$ in CW-pulsed mode. A resolution enhancement up to a factor of $\xi = 3$ was achieved, track spot sizes were measured to have widths down to $\Delta x = 110nm$. This was the first time that STED imaging of FNTD samples has been performed successfully.

Discussion & Outlook

5

5.1 Laser Diodes in STED Nanoscopy

Based on preceding work [24] the potential of high power Fabry-Pérot laser diodes as STED laser was examined. The most important parameter for the resolution in STED is the pulse energy E_p of the STED laser, which is delivered within one lifetime τ_s of the targeted fluorophore. The numerical analysis of LDs has shown that upon the injection of strong current pulses the emission from the diode closely follows temporal shape of the current pulse. Consequently an electronic circuitry generating current pulses with peak currents $I_{peak} > 1A$ of duration $\tau_p < 3ns$ was required.
The developed circuitry yielded $I_{peak} \approx 1.5A$ in $\tau_p \approx 2ns$. This enabled pulse energies up to $E_p = 2.3nJ$. In order to supply even more laser power to the STED setup, two of these laser diodes with crossed polarizations were merged. This was possible due to the utilization of the easySTED method. Technical samples could be imaged with a resolution of $\Delta x = 50nm$. Since the STED pulses were almost as long as the fluorescence lifetime, time gating yielded a great enhancement of image quality. Although the resolution was similar for ungated images, the diffraction limited signal which contributes to the background leads to poor contrast in ungated images. The obtained resolution was limited by laser power, which in turn was limited by the current strength of the pulsing electronics. This was even more pronounced for the imaging of biological samples. Due to the shorter fluorescence lifetime of the fluorophores which were observed there, the laser pulse energy contained in the $\tau_p = 2ns$ LD pulses could not be used as effectively as was the case for shorter pulses. Nevertheless, the findings clearly demonstrate that Fabry-Pérot laser diodes can be employed to create a low-effort high-performance STED nanoscope.

5.1.1 Electro-Optical Considerations

Higher currents in shorter pulses than the ones achieved demand for more elaborate electro optical circuit integration, as the following consideration demonstrates. In designing the PCB layout for the laser diodes care was taken of minimizing parasitic inductance by long leads. The wire connectors of the diode itself, however, had to be used. The two wires amount to an inductance of $L_{par} = 2 \times 5nH$ [135]. A

SPICE simulation of the employed transistor with and without these inductances in series with the load was carried out. The result is shown in figure 5.1 . Already these low inductance values lead to a significantly lower peak current I_{peak} and a distorted pulse is obtained if $\tau_I = 2.5ns$ current pulses are applied. There are publications in which transistors, capacitors and laser diode have been mounted onto one substrate in close vicinity to eliminate parasitic inductance and capacity effects [70, 105]. This is, however, not possible to achieve with commercially available laser diodes. Still, the papers demonstrate that these electronic aspects are merely technical hurdles that can be overcome.

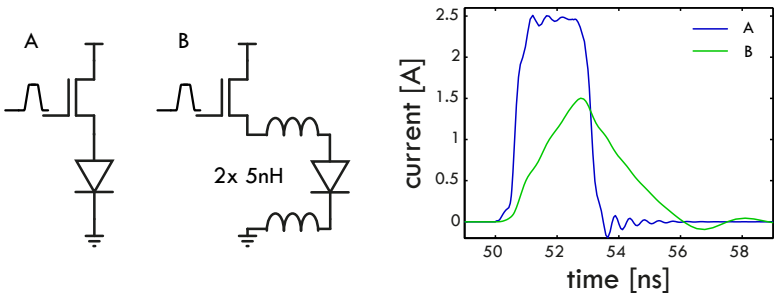

Figure 5.1.: Simulation of the effect of parasitic inductances. The leads of a commercial LD in a $5.6mm$ package already feature these inductance values, implying high frequency signal inhibition.

If going to higher currents is possible, the next issue which arises are the laser diode facet intensities allowed before catastrophic optical damage occurs. One has to consider two cases there. At low repetition rates, where the average power stays below the specified CW power the peak intensity and the respective power P_{th} during the pulse has to stay below the damage threshold. For pulse lengths between $1\mu s$ and $1ns$ this threshold roughly rises according to the square root law, $P_{th} \propto \tau_p^{-1/2}$ [115]. To obtain an estimated value for P_{th} one can start at $\tau_p = 1\mu s$ with the CW power of $P = 120mW$ for the examined diodes. This yields $P_{th} = 3.8W$ for $\tau_p = 1ns$, corresponding to $E_p = 3.8nJ$. Two of these diodes merged as presented could amount to a STED pulse energy of $E_p > 7nJ$. The second case to consider emerges at repetition rates ν_L where this pulse energy results in average powers higher than the specified CW power. Then the average power instead of the peak power would become the limiting factor. For the estimated case this would mean $\nu_L < 32MHz$, which is acceptable for STED. Up to this repetition rate an increase in pulse energy by a factor of 2.5 as compared to the presented STED results would be possible. According to this estimation a resolution of $\Delta x \approx 30nm$ could be achieved with these laser diodes, which makes

them highly attractive STED lasers.

5.1.2 Wavelength Considerations

A STED laser system based on commercial $660nm$ laser diodes has been presented which can address red emitting fluorophores. Another popular class of STED fluorophores absorbs at red wavelengths and emits in the near infrared [136–138]. Consequently, a STED laser emitting between $750nm$ and $800nm$ is required. On the one hand this led to the tapered amplifier approach, which will be discussed in the next section. Apart from that, recently laser diodes have become commercially available which deliver $P = 800mW$ in CW mode at a wavelength of $800nm$ [139]. They seemed promising for application in STED. Despite the higher CW specification they delivered $E_p = 2nJ$ in pulsed mode, which is not more pulse energy than achieved with the $660nm$ diodes. The simulations carried out in section 3.2 provide an explanation for this. The laser pulse shape closely follows the injected current pulse, with a peak power according to the differential efficiency η_x. This parameter is $\eta_{IR} = 0.8W/A$ for the infrared and $\eta_{red} = 1W/A$ for the red laser diodes [90,140]. The difference can mainly be attributed to the difference in photon energy. Thus, the photon yield, as the relevant parameter for STED is similar for both LD types. Accordingly, for the diodes at $800nm$ the same challenges apply as for the $660nm$ LDs. If high currents can be generated, these high power SM laser diodes promise to sustain higher facet intensities. The same estimation as above yields $P_{th} > 20W$ and $E_p > 20nJ$, respectively. In that case the current pulse generation would probably be the limiting factor again, since $I_{peak} > P_{th}/\eta_{IR} = 25A$ would be required. Nonetheless, supplied with high power current drivers, these devices are promising laser sources for STED nanoscopy, as well.
Apart from the challenges present to semiconductor STED lasers, semiconductor excitation lasers have also faced a constraint in their applicability to STED. The reason for this has been the green-yellow gap of laser diodes. So far no ps pulse emitting laser diode with wavelengths between $520nm$ and $620nm$ had been available. The laser module presented in this work, available with $\lambda = 532nm$, $561nm$ and $594nm$ has greatly improved this situation. The modules are ideal sources for fluorescence excitation at these wavelengths, not only applicable with STED but all other fluorescence techniques, particularly including fluorescence lifetime applications. To our knowledge so far there has been no publication reporting on a semiconductor source of ps pulses between $550nm$ and $600nm$.

5.2 Tapered Amplifiers in STED Nanoscopy

Due to the limitations found for laser diodes as STED lasers, finally originating from their narrow emitting facets, a semiconductor tapered amplifier system has been tailored for the purposes of STED nanoscopy. The wavelength of the employed amplifier was $767nm$, nevertheless the obtained results are similarly valid for any wavelength at which tapered amplifiers are available. The pulse characteristics which could be reached with the TA pulses were superior to those of a FP laser diode. Twice the pulse energy, $E_p = 2.8nJ$ was obtained in pulses half as long, i.e. $\tau_p < 1ns$[1]. Since in the LD STED setup two devices were employed to combine to the STED laser, the resolution enhancement was similar for the two presented STED systems, $\Delta x = 60nm$ was obtained from the TA STED system. This resolution was limited by available pulse energy. A suspicion that the broad spectrum of the ASE lead to filling of the intensity zero was ruled out by explicitly cleaning up the TA light with another filter of the type LL01-785, which suppresses sidebands outside its $5nm$ pass-band by three orders of magnitude. This did not yield significantly different results, proving that the ASE does neither help quenching, due to its broad temporal spread, nor does it deteriorate the intensity zero. Furthermore, the obtained resolution agrees very well with those obtained with a similar setup which utilizes a different kind of laser. In that case $E_p \approx 1nJ$ in the focus was necessary for a resolution of $60nm$ [141].
There were mainly two challenges to reaching higher pulse energies from the pulsed tapered amplifier. The first was the generation and especially the delivery of multi-ampere currents in a pulses of a few nanoseconds. The shortest current pulses generated in the commercial TA had a pulse width of $\tau_I \approx 4ns$. In the electro-mechanical design of the two-contacts TA attention was paid to keeping leads at the core of the switching circuitry as short as possible, cf. figure A.3 . This way pulses with $\tau_I < 3ns$ were obtained, but the peak current could not be increased. As explained in the discussion on STED laser diodes, improving the electronic properties, in particular increasing the current, requires electro-optical integration. If currents between 15 and $20A$ were possible, as in [105], extrapolation of the evolution of the pulse energy in figure 3.6 a) yields a fiber coupled pulse energy beyond $10nJ$.
When the data of figure 3.6 a) is reconsidered, however, the increasing ASE emerges as the second challenge for high pulse energy TA lasers. The investigations employing a two-contacts tapered amplifier chip, in which RW section and taper section could be supplied separately with current, have shown that the ASE contribution is increased if the current through the RW section increases. This is due to seed

[1] This comparison was made between fiber coupled laser power of each device. Also, ASE contribution was not taken into account.

competition: The photons which are spontaneously emitted in the waveguide section act as seed for the taper section, thus depleting carriers which are then no longer available for depletion by the intended seed. Similar results have been reported for a TA MOPA system where the TA was DC driven [101]. Consequently, if high output powers with low ASE contribution are approached with a TA, the separate control of the different sections is important.

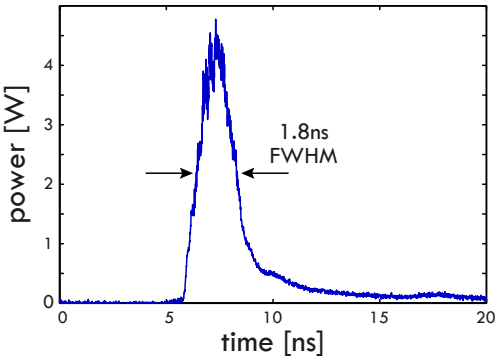

Figure 5.2.: $10nJ$ pulse from two-contacts TA in CW-pulsed mode. Pulses like this are well suited for STED nanoscopy as has been demonstrated for the case of LD pulses.

Interestingly the seed competition is not observed with this symptoms in CW-pulsed mode. This can be explained by the fact that ASE is suppressed by the permanent presence of seed light. This is comparable to the CW case, where ASE is typically suppressed three to four orders of magnitude as compared to the amplified seed [142, 143]. Further investigations with the two-contacts TA showed that as a result of the short current pulses in the taper section short optical pulses could be generated in CW-pulsed mode, as well. The single contact TA delivered pulse energies of $E_p = 28nJ$ in a $\tau_p = 10ns$ pulse, which could not be shortened due to electronic restrictions. The two-contacts TA, on the other hand, delivered a pulse with $E_p = 10nJ$ and a width of $\tau_p = 1.8ns$, as is shown in figure 5.2. Such pulses are promising if employed for STED with popular organic fluorophores which possess a lifetime of a few nanoseconds. This demonstrates that other approaches than a pulsed seed could finally have a higher yield, since the problem of ASE is avoided. In fact, a very recent publication has demonstrated nanosecond pulsed semiconductor emission under very similar conditions. A CW seed source was used together with a multi-section tapered device, the sections of which were supplied with current separately. This arrangement yielded pulses with $\tau_p = 2.5ns$ and $E_p > 20nJ$. The ASE contribution to the total pulse energy was reported to be 1% [144].

Semiconductor lasers which include amplifier devices have been demonstrated to enable pulsing at energies exceeding those obtained from simpler semiconductor lasers. Accordingly, the achieved resolution enhancement per device was higher. Since these lasers still possess all advantages of semiconductor lasers regarding pulse synchronization, compactness and availability, they are highly attractive STED lasers. This is enhanced by the indications that the pulse energies from such semiconductor laser architectures can still be increased.

5.3 TA STED FNTD Imaging

Apart from organic dye samples the TA STED system was used with samples containing another class of fluorophores. Fluorescent nuclear track detectors feature color centers which fit the spectral properties of the TA system. Due to the flexibility of this STED laser an operational mode could be found which for the first time allowed to resolve ion track spots in an FNTD down to $100nm$ (FWHM). This was achieved at a pulse energy of $E_p = 3.9nJ$ in the focus, indicating that the stimulated emission cross section of these fluorophores is significantly lower than for typical organic dyes.

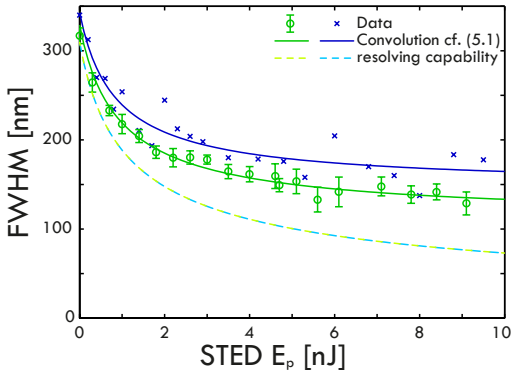

Figure 5.3.: Evaluation of FNTD STED imaging. Two data sets were evaluated. An FNTD irradiated with C^{6+} ions of energy $224.8MeV/u$ yielded the blue data points. Irradiation with protons of energy $49MeV$ yielded the green data where ten track spots were evaluated per pulse energy. The resolving capability extracted from the data coincides for the two data sets, justifying the model (5.1).

An important issue, however, is whether this resolution was power limited. The actual size of the fluorescently activated region is not known from other experiments, therefore it is possible that the resolved size already is the track spot size. In order to examine this more thoroughly a series of measurements was carried

out in which the the STED pulse energy was sequentially increased and the resulting resolution Δx_{ef} was measured. If a point-like object is observed, the data is expected to resemble equation (2.10), i.e. $\Delta x_{ef} = \Delta x$. If, on the other hand, an object of size Δx_{obj} is observed, the measured width of this object is[2]

$$\Delta x_{ef} = \sqrt{(\Delta x_{obj})^2 + (\Delta x)^2}. \tag{5.1}$$

As a matter of fact, equation (2.10) could not be fitted plausibly to the measured data. A fit of type (5.1) is shown in figure 5.3 for two different data sets. Fit parameters were Δx_{obj} and the saturation pulse energy E_{sat}. The obtained object widths were $\Delta x_{obj} = 147nm$ and $\Delta x_{obj} = 110nm$. Furthermore, the actually possible resolving capability can be evaluated with the knowledge of E_{sat}. Interestingly, both data sets yield almost identical curves for the resolution capability, as should be, with a maximum possible resolution of $\Delta x \approx 75nm$. This is clearly below the size to which the track spots could be resolved. These facts combined are interpreted as a strong indication that the true width of the track spots was determined, which has so far been impossible for carbon ions and protons.

5.4 Future Directions for SC Lasers in STED Nanoscopy

Figure 5.4 depicts a comparison of STED laser types with regard to cost, performance and system complexity including the results of this thesis. Before the work for this thesis was started, the lasers which could be employed for STED nanoscopy were not tailored for this application. Therefore, big efforts were involved in running a STED system successfully. Complex solutions for temporal and spatial beam shaping, as well as laborious pulse synchronization were frequent challenges.

Pulsed semiconductor lasers, on the other hand, which do not show these disadvantages, were similarly inapt as STED lasers, because in their development attention was especially put to pulse widths below $100ps$, such that the resulting pulse energies were in the pJ range, or they were available with pulse lengths of several tens of ns. This thesis has demonstrated that semiconductor lasers can be operated in a mode which is ideally suited for STED. Different commercially available semiconductor laser architectures were analyzed in this mode, and pulses with durations of $0.5ns$ - $2ns$ and pulse energies of up to $10nJ$ were obtained, enabling a fivefold resolution enhancement.

The presented laser diode STED system which is based on DVD-drive laser diodes

[2]This is for the case that both, imaging PSF and object can be described by a two dimensional Gaussian. Relation (5.1) gives the width of the convolution of two Gaussians with the respective widths.

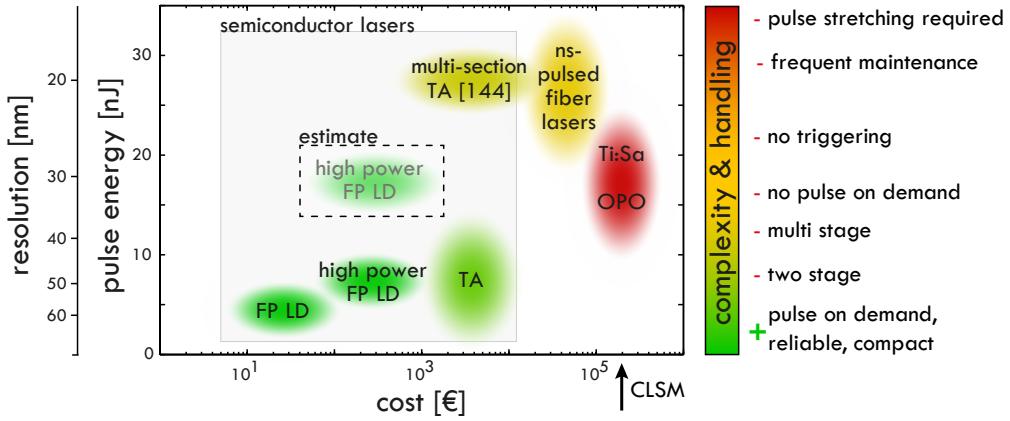

Figure 5.4.: Comparison of the performance of different STED laser types. Encoded in color the graphic indicates technical disadvantages which the repective laser type bears. It is obvious that in this regard semiconductor lasers and in particular FP LD are first choice, as well as concerning the cost. The shaded box frames all semiconductor lasers shown in the graphic. The extent of the box can be considered the full potential of semiconductor lasers for STED nanoscopy, outperforming many other STED laser systems.

equipped with powerful pulsing electronics, enabled imaging with resolutions down to $50nm$. The insight gained during the work on these diodes could be used to develop a semiconductor based *ps*-pulsing laser source at wavelengths bridging the green-yellow gap. Such a laser ideally complemented the diode STED lasers as excitation lasers.
In recent years, apart from these developments on semiconductor lasers *ns*-pulsed fiber lasers have come up with pulse energies of about $30nJ$, making them well suited for STED. A very recent publication, [144], indicates that semiconductor devices similar to the ones presented in this thesis are capable of generating equally powerful pulses. Due to its advantages in compactness and control, such a laser would be even more attractive for STED than the fiber lasers. Most importantly, this analysis shows that in the future the STED laser will no longer be the component which limits the availability of STED nanoscopy for life scientists.

Appendix A

A.1 CW Laser Diode Simulations

Some of the parameters which were put into the simulations were supplied by the manufacturer, explicitly for the used diode. Length and width of the semiconductor active region are

$$L = 1540\mu m \quad \text{and} \quad W = 2\mu m,$$

respectively. Furthermore the device uses three quantum wells (QW). With a width of about $15nm$ per QW,

$$V \approx 140\mu m^3$$

is obtained. The facet reflectivities are $R_f = 0.93$ and $R_r = 0.06$. The photon lifetime τ_c in the cavity is given by [88]

$$\frac{1}{\tau_c} = \frac{2L}{c} \log\left(\frac{1}{R_f R_r}\right) + c\alpha, \tag{A.1}$$

where c is the speed of light in the medium and α is a factor accounting for the internal losses. The first part can be evaluated using the reflectivities. This yields $\tau_c < 10ps$, giving the range in which it was finally chosen by using the value at which the slope efficiency of $1.1W/A$ was matched, cf. figure A.1 c). Furthermore transparency density and the time constant of spontaneous recombination where chosen such that the simulation yielded the specified threshold current of $I_{th} \approx 60mA$. Parameters other than the manufaturer supplied and the fitted ones were taken from [81], [82], and [88]

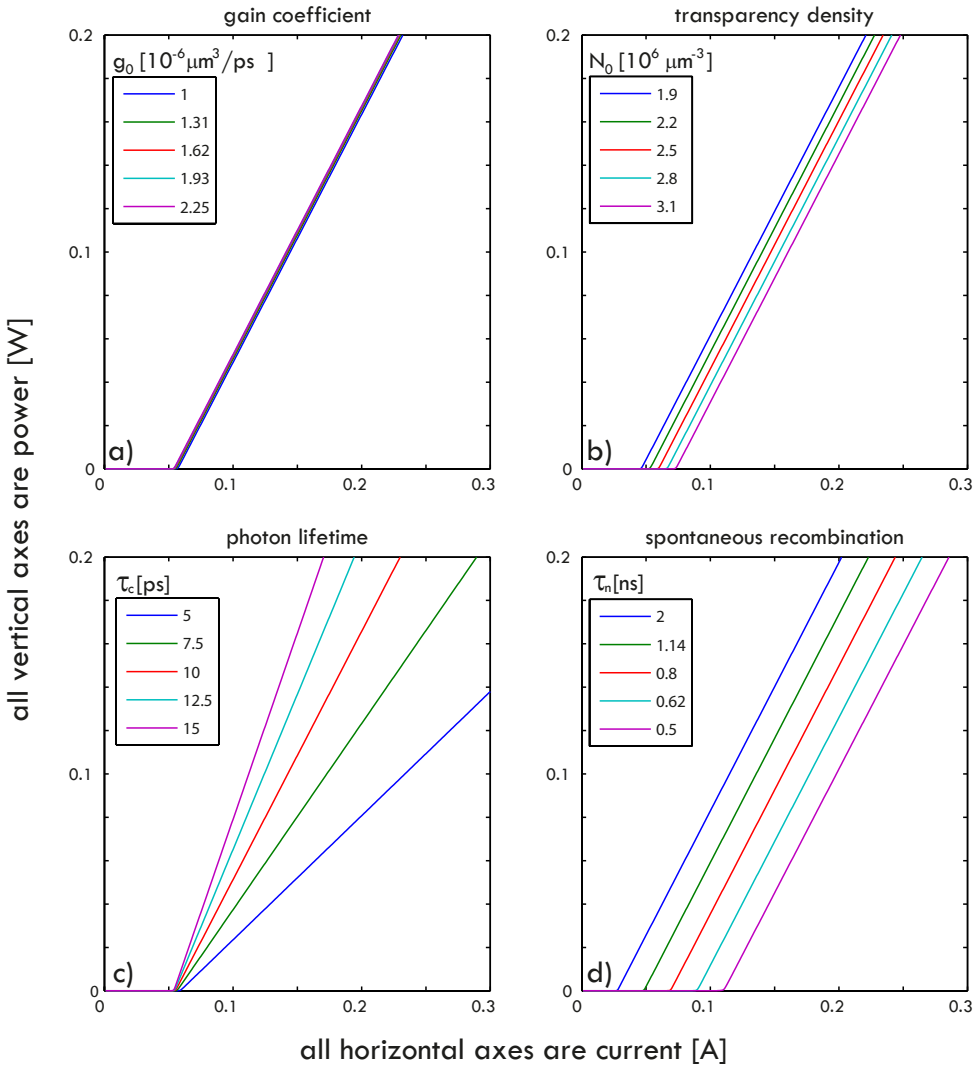

Figure A.1.: Simulation of current characteristic of laser diode.

A.2 Picosecond Pulses at 594nm

A laser module emitting at a wavelength of $\lambda = 594nm$ (QD593-9450, QD Laser Inc.) was operated in the same way as described in section 3.4. Figure A.2 shows a a recorded pulse train at $\nu_L = 80MHz$ and a enlarged single pulse which was recorded to a pulse width $\tau_p < 60ps$ which is close to the measureable limit, since a oscilloscope with a bandwidth of $12GHz$ was employed for the recordings of the signal from a PD with a bandwidth of $20GHz$. The pulse energy was $E_p = 1.8pJ$, which was, however not limited by the laser module.

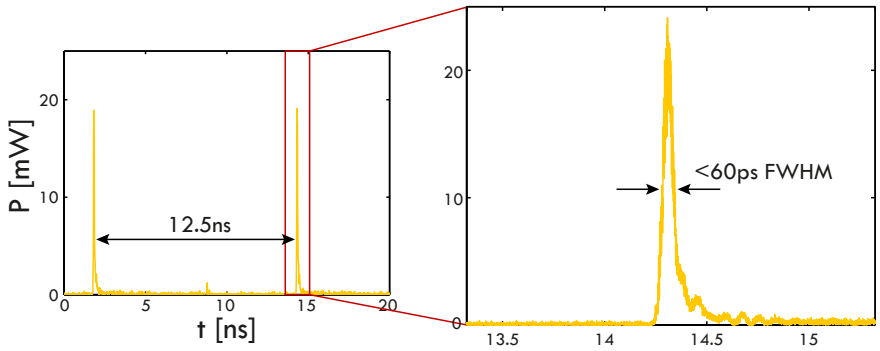

Figure A.2.: *ps* pulses from an all semiconducto laser module at $\lambda = 594nm$.

A.3 Two-Contacts TA

Electronic integration of the TA

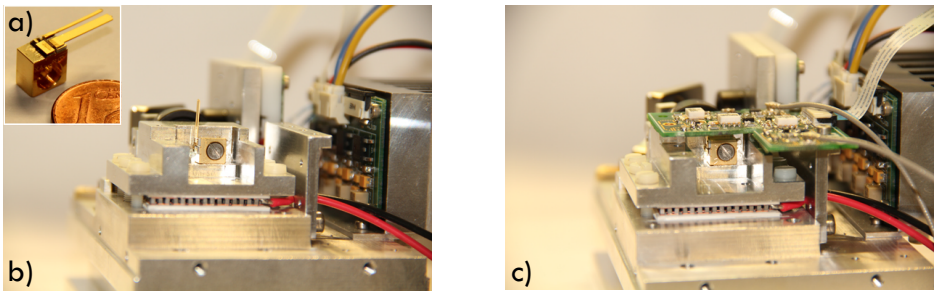

Figure A.3.: TA electronic integration. a) The unmounted Two-Contacts TA. The actual semicondctor chip resides on top of the gold plated C-Mount. The two flags to the right are the contacts to the anodes of RW and taper section. b) Mounted TA without PCB. In the background the mount for the seed diode can be seen. c) PCB mounted. The flags could be soldered directly to the PCB, thereby avoiding unnecessary leads which generate parasitic electric capacities and inductances.

A.4 Publications and Conference Contributions

M. Henrich, J. Engelhardt, S.W. Hell, "All semiconductor laser approach for STED nanoscopy", conference talk, *Photonics West 2013 symposium*, San Francisco, USA, Feb. 2013.

M. Henrich, "Gepulste Laserlichtquelle für die Fluoreszenzanregung", Gebrauchsmusteranmeldung (utility model application) 20 2013 006 817.5, 2013.

List of Figures

Constants & Unit Prefixes

c	Speed of light, $c = 299\ 792\ 458 m/s$
e	Elementary charge, $e = 1.602 \cdot 10^{-19} C$
eV	Electron Volt, $1eV = 1.602 \cdot 10^{-19} J$, wavelength of a photon of energy $2eV$: $\lambda = \frac{hc}{2eV} = 619.92nm$
h	Planck's constant, $h = 6.626 \cdot 10^{-34} J/s$

f	$\times 10^{-15}$
p	$\times 10^{-12}$
n	$\times 10^{-9}$
μ	$\times 10^{-6}$
m	$\times 10^{-3}$
k	$\times 10^{3}$
M	$\times 10^{6}$
G	$\times 10^{9}$
T	$\times 10^{12}$

Bibliography

[1] E. Abbe, "Beiträge zur Theorie des Mikroskops und der mikroskopischen Wahrnehmung," *Archiv für mikroskopische Anatomie*, vol. 9, pp. 413–418, Dec. 1873.

[2] M. Minsky, "Memoir on inventing the confocal scanning microscope," *Scanning*, vol. 10, no. 4, p. 128–138, 1988.

[3] W. Lukosz and M. Marchand, "Optische Abbildung unter Überschreitung der beugungsbedingten Auflösungsgrenze," *Optica Acta: International Journal of Optics*, vol. 10, no. 3, pp. 241–255, 1963.

[4] S. Hell and E. H. K. Stelzer, "Properties of a 4Pi confocal fluorescence microscope," *Journal of the Optical Society of America A*, vol. 9, pp. 2159–2166, Dec. 1992.

[5] G. Binnig, C. F. Quate, and C. Gerber, "Atomic Force Microscope," *Physical Review Letters*, vol. 56, pp. 930–933, Mar. 1986.

[6] U. Dürig, D. W. Pohl, and F. Rohner, "Near-field optical-scanning microscopy," *Journal of Applied Physics*, vol. 59, pp. 3318–3327, May 1986.

[7] R. Erni, M. D. Rossell, C. Kisielowski, and U. Dahmen, "Atomic-Resolution Imaging with a Sub-50-pm Electron Probe," *Physical Review Letters*, vol. 102, p. 096101, Mar. 2009.

[8] S. W. Hell and J. Wichmann, "Breaking the diffraction resolution limit by stimulated emission: stimulated-emission-depletion fluorescence microscopy," *Optics Letters*, vol. 19, pp. 780–782, June 1994.

[9] S. W. Hell and M. Kroug, "Ground-state-depletion fluorscence microscopy: A concept for breaking the diffraction resolution limit," *Applied Physics B*, vol. 60, pp. 495–497, May 1995.

[10] T. A. Klar and S. W. Hell, "Subdiffraction resolution in far-field fluorescence microscopy," *Optics Letters*, vol. 24, pp. 954–956, July 1999.

[11] T. A. Klar, S. Jakobs, M. Dyba, A. Egner, and S. W. Hell, "Fluorescence microscopy with diffraction resolution barrier broken by stimulated emission," *Proceedings of the National Academy of Sciences*, vol. 97, pp. 8206–8210, July 2000. PMID: 10899992.

[12] J. Fölling, M. Bossi, H. Bock, R. Medda, C. A. Wurm, B. Hein, S. Jakobs, C. Eggeling, and S. W. Hell, "Fluorescence nanoscopy by ground-state depletion and single-molecule return," *Nature Methods*, vol. 5, pp. 943–945, Nov. 2008.

[13] E. Betzig, G. H. Patterson, R. Sougrat, O. W. Lindwasser, S. Olenych, J. S. Bonifacino, M. W. Davidson, J. Lippincott-Schwartz, and H. F. Hess, "Imaging Intracellular Fluorescent Proteins at Nanometer Resolution," *Science*, vol. 313, pp. 1642–1645, Sept. 2006. PMID: 16902090.

[14] M. J. Rust, M. Bates, and X. Zhuang, "Sub-diffraction-limit imaging by stochastic optical reconstruction microscopy (STORM)," *Nature Methods*, vol. 3, pp. 793–796, Oct. 2006.

[15] M. Bossi, J. Fölling, M. Dyba, V. Westphal, and S. W. Hell, "Breaking the diffraction resolution barrier in far-field microscopy by molecular optical bistability," *New Journal of Physics*, vol. 8, p. 275, Nov. 2006.

[16] K. Xu, H. P. Babcock, and X. Zhuang, "Dual-objective STORM reveals three-dimensional filament organization in the actin cytoskeleton," *Nature Methods*, vol. 9, pp. 185–188, Feb. 2012.

[17] F. Göttfert, C. Wurm, V. Mueller, S. Berning, V. Cordes, A. Honigmann, and S. Hell, "Coaligned Dual-Channel STED Nanoscopy and Molecular Diffusion Analysis at 20 nm Resolution," *Biophysical Journal*, vol. 105, pp. L01–L03, July 2013.

[18] U. V. Nägerl, K. I. Willig, B. Hein, S. W. Hell, and T. Bonhoeffer, "Live-cell imaging of dendritic spines by STED microscopy," *Proceedings of the National Academy of Sciences*, vol. 105, pp. 18982–18987, Feb. 2008. PMID: 19028874.

[19] S. Berning, K. I. Willig, H. Steffens, P. Dibaj, and S. W. Hell, "Nanoscopy in a Living Mouse Brain," *Science*, vol. 335, pp. 551–551, Mar. 2012. PMID: 22301313.

[20] R. R. Kellner, C. J. Baier, K. I. Willig, S. W. Hell, and F. J. Barrantes, "Nanoscale organization of nicotinic acetylcholine receptors revealed by stimulated emission depletion microscopy," *Neuroscience*, vol. 144, pp. 135–143, Jan. 2007.

[21] W. Lin, R. Margolskee, G. Donnert, S. W. Hell, and D. Restrepo, "Olfactory neurons expressing transient receptor potential channel M5 (TRPM5) are involved in sensing semiochemicals," *Proceedings of the National Academy of Sciences*, vol. 104, pp. 2471–2476, Feb. 2007. PMID: 17267604.

[22] B. Hein, K. I. Willig, and S. W. Hell, "Stimulated emission depletion (STED) nanoscopy of a fluorescent protein-labeled organelle inside a living cell," *Proceedings of the National Academy of Sciences*, vol. 105, pp. 14271–14276, Sept. 2008. PMID: 18796604.

[23] T. Suhara, *Semiconductor Laser Fundamentals*. CRC Press, Mar. 2004.

[24] S. Schrof, T. Staudt, E. Rittweger, N. Wittenmayer, T. Dresbach, J. Engelhardt, and S. W. Hell, "STED nanoscopy with mass-produced laser diodes," *Optics Express*, vol. 19, pp. 8066–8072, Apr. 2011.

[25] S. W. Hell, "Microscopy and its focal switch," *Nature Methods*, vol. 6, pp. 24–32, Jan. 2009.

[26] D. Wildanger, B. R. Patton, H. Schill, L. Marseglia, J. P. Hadden, S. Knauer, A. Schönle, J. G. Rarity, J. L. O'Brien, S. W. Hell, and J. M. Smith, "Solid Immersion Facilitates Fluorescence Microscopy with Nanometer Resolution and Sub-Ångström Emitter Localization," *Advanced Materials*, p. n/a–n/a, 2012.

[27] B. Richards and E. Wolf, "Electromagnetic Diffraction in Optical Systems. II. Structure of the Image Field in an Aplanatic System," *Proceedings of the Royal Society of London. Series A. Mathematical and Physical Sciences*, vol. 253, pp. 358–379, Dec. 1959.

[28] E. Wolf, "Electromagnetic Diffraction in Optical Systems. I. An Integral Representation of the Image Field," *Proceedings of the Royal Society of London. Series A. Mathematical and Physical Sciences*, vol. 253, pp. 349–357, Dec. 1959.

[29] M. Born, A. B. Bhatia, and E. Wolf, *Principles of optics: electromagnetic theory of propagation, interference and diffraction of light*. Cambridge [u.a.: Cambridge Univ. Press, 2010.

[30] B. E. A. Saleh, *Fundamentals of photonics*. Wiley series in pure and applied optics, Hoboken, N.J: Wiley Interscience, 2nd ed ed., 2007.

[31] J. Pawley (Ed.), ed., *Handbook of Biological Confocal Microscopy*. Springer Heidelberg,Berlin, 3 ed., 2006.

[32] H. Zollinger, *Color Chemistry: Syntheses, Properties, and Applications of Organic Dyes and Pigments*. John Wiley & Sons, 2003.

[33] S. W. Hell, K. I. Willig, M. Dyba, S. Jakobs, L. Katrup, and V. Westphal, "Nanoscale Resolution With Focused Light: Stimulated Emission Depletion and Other Reversible Saturable Optical Fluorescence Transitions Microscopy Concepts," in *Handbook of Biological Confocal Microscopy*, Berlin, Heidelberg: Springer, 2006.

[34] S. W. Hell, "Strategy for far-field optical imaging and writing without diffraction limit," *Physics Letters A*, vol. 326, pp. 140–145, May 2004.

[35] S. W. Hell, "Far-Field Optical Nanoscopy," *Science*, vol. 316, pp. 1153–1158, May 2007. PMID: 17525330.

[36] A. Einstein, "Strahlungs-Emission und Absorption nach der Quantentheorie," *Deutsche Physikalische Gesellschaft*, vol. 18, pp. 318–323, 1916.

[37] A. Einstein, "Zur Quantentheorie der Strahlung," *Physikalische Zeitschrift*, vol. 18, pp. 121–128, 1917.

[38] V. Westphal and S. W. Hell, "Nanoscale Resolution in the Focal Plane of an Optical Microscope," *Physical Review Letters*, vol. 94, p. 143903, Apr. 2005.

[39] T. A. Klar, E. Engel, and S. W. Hell, "Breaking Abbe's diffraction resolution limit in fluorescence microscopy with stimulated emission depletion beams of various shapes," *Physical Review E*, vol. 64, p. 066613, Nov. 2001.

[40] J. Keller, A. Schönle, and S. W. Hell, "Efficient fluorescence inhibition patterns for RESOLFT microscopy," *Optics Express*, vol. 15, pp. 3361–3371, Mar. 2007.

[41] B. Harke, J. Keller, C. K. Ullal, V. Westphal, A. Schönle, and S. W. Hell, "Resolution scaling in STED microscopy," *Optics Express*, vol. 16, pp. 4154–4162, Mar. 2008.

[42] C. Kempf, T. Staudt, P. Bingen, H. Horstmann, J. Engelhardt, S. W. Hell, and T. Kuner, "Tissue Multicolor STED Nanoscopy of Presynaptic Proteins in the Calyx of Held," *PLoS ONE*, vol. 8, p. e62893, Apr. 2013.

[43] M. Reuss, J. Engelhardt, and S. W. Hell, "Birefringent device converts a standard scanning microscope into a STED microscope that also maps molecular orientation," *Optics Express*, vol. 18, pp. 1049–1058, Jan. 2010.

[44] P. Bingen, M. Reuss, J. Engelhardt, and S. W. Hell, "Parallelized STED fluorescence nanoscopy," *Optics Express*, vol. 19, pp. 23716–23726, Nov. 2011.

[45] J. Engelhardt, J. Keller, P. Hoyer, M. Reuss, T. Staudt, and S. W. Hell, "Molecular Orientation Affects Localization Accuracy in Superresolution Far-Field Fluorescence Microscopy," *Nano Letters*, vol. 11, pp. 209–213, Jan. 2011.

[46] M. Dyba, T. A. Klar, S. Jakobs, and S. W. Hell, "Ultrafast dynamics microscopy," *Applied Physics Letters*, vol. 77, pp. 597–599, July 2000.

[47] J. R. Moffitt, C. Osseforth, and J. Michaelis, "Time-gating improves the spatial resolution of STED microscopy," *Optics Express*, vol. 19, pp. 4242–4254, Feb. 2011.

[48] G. Vicidomini, G. Moneron, K. Y. Han, V. Westphal, H. Ta, M. Reuss, J. Engelhardt, C. Eggeling, and S. W. Hell, "Sharper low-power STED nanoscopy by time gating," *Nature Methods*, vol. 8, no. 7, pp. 571–573, 2011.

[49] G. Vicidomini, I. Coto Hernández, M. d'Amora, F. Cella Zanacchi, P. Bianchini, and A. Diaspro, "Gated CW-STED microscopy: A versatile tool for biological nanometer scale investigation," *Methods*, 2013.

[50] G. Vicidomini, A. Schönle, H. Ta, K. Y. Han, G. Moneron, C. Eggeling, and S. W. Hell, "STED Nanoscopy with Time-Gated Detection: Theoretical and Experimental Aspects," *PLoS ONE*, vol. 8, p. e54421, Jan. 2013.

[51] V. Westphal, J. Seeger, T. Salditt, and S. W. Hell, "Stimulated emission depletion microscopy on lithographic nanostructures," *Journal of Physics B: Atomic, Molecular and Optical Physics*, vol. 38, p. S695, May 2005.

[52] M. Leutenegger, C. Ringemann, T. Lasser, S. W. Hell, and C. Eggeling, "Fluorescence correlation spectroscopy with a total internal reflection fluorescence STED microscope (TIRF-STED-FCS)," *Optics Express*, vol. 20, pp. 5243–5263, Feb. 2012.

[53] G. Vicidomini, G. Moneron, C. Eggeling, E. Rittweger, and S. W. Hell, "STED with wavelengths closer to the emission maximum," *Optics Express*, vol. 20, pp. 5225–5236, Feb. 2012.

[54] C. H. Townes, "The First Laser," in *A century of nature twenty-one discoveries that changed science and the world*, Chicago: University of Chicago Press, 2003.

[55] G. Overton, A. Nogee, and C. Holton, "LASER MARKETPLACE 2014: Lasers forge 21st century innovations," *Laser Focus World Magazine*, 2014.

[56] N. Basov, O. Krokhin, and Y. Popov, "The possibility of use of indirect transitions to obtain negative temperature in semiconductors," *Journal of Experimental and Theoretical Physics*, vol. 12, p. 1033, 1961.

[57] Z. I. Alferov, "Nobel Lecture: The double heterostructure concept and its applications in physics, electronics, and technology," *Reviews of Modern Physics*, vol. 73, pp. 767–782, Oct. 2001.

[58] T. H. Maiman, "Stimulated Optical Radiation in Ruby," *Nature*, vol. 187, pp. 493–494, Aug. 1960.

[59] R. N. Hall, G. E. Fenner, J. D. Kingsley, T. J. Soltys, and R. O. Carlson, "Coherent Light Emission From GaAs Junctions," *Physical Review Letters*, vol. 9, pp. 366–368, Nov. 1962.

[60] D. Welch, "A brief history of high-power semiconductor lasers," *IEEE Journal of Selected Topics in Quantum Electronics*, vol. 6, pp. 1470–1477, Nov. 2000.

[61] C. K. Kao, "Nobel Lecture: Sand from centuries past: Send future voices fast," *Reviews of Modern Physics*, vol. 82, pp. 2299–2303, Aug. 2010.

[62] M. J. Connelly, *Semiconductor Optical Amplifiers*. Springer, Jan. 2002.

[63] M. Wuttig and N. Yamada, "Phase-change materials for rewriteable data storage," *Nature Materials*, vol. 6, pp. 824–832, Nov. 2007.

[64] J. Welte, I. Steinke, M. Henrich, F. Ritterbusch, M. K. Oberthaler, W. Aeschbach-Hertig, W. H. Schwarz, and M. Trieloff, "Hyperfine spectroscopy of the 1s5−2p9 transition of A39r," *Review of Scientific Instruments*, vol. 80, p. 113109, Nov. 2009.

[65] V. Westphal, C. M. Blanca, M. Dyba, L. Kastrup, and S. W. Hell, "Laser-diode-stimulated emission depletion microscopy," *Applied Physics Letters*, vol. 82, pp. 3125–3127, Apr. 2003.

[66] L. A. Coldren and S. W. Corzine, *Diode lasers and photonic integrated circuits*. New York [u.a.: Wiley, 1995.

[67] P. Vasilev, *Ultrafast diode lasers: fundamentals and applications*. Boston: Artech House, 1995.

[68] P. Paulus, R. Langenhorst, and D. Jager, "Generation and optimum control of picosecond optical pulses from gain-switched semiconductor lasers," *IEEE Journal of Quantum Electronics*, vol. 24, no. 8, pp. 1519–1523, 1988.

[69] L. E. Adams, M. Ramaswamy, U. Keller, M. T. Asom, J. G. Fujimoto, and E. S. Kintzer, "Mode locking of a broad-area semiconductor laser with a multiple-quantum-well saturable absorber," *Optics Letters*, vol. 18, pp. 1940–1942, Nov. 1993.

[70] S. Schwertfeger, A. Klehr, T. Hoffmann, A. Liero, H. Wenzel, and G. Erbert, "Picosecond pulses with 50 W peak power and reduced ASE background from an all-semiconductor MOPA system," *Applied Physics B: Lasers and Optics*, vol. 103, no. 3, pp. 603–607, 2011.

[71] M. J. Strain, M. Zanola, G. Mezösi, and M. Sorel, "Ultrashort Q-switched pulses from a passively mode-locked distributed Bragg reflector semiconductor laser," *Optics Letters*, vol. 37, pp. 4732–4734, Nov. 2012.

[72] G. J. Lasher, "Analysis of a proposed bistable injection laser," *Solid-State Electronics*, vol. 7, pp. 707–716, Oct. 1964.

[73] H. Wenzel, G. Erbert, and P. Enders, "Improved theory of the refractive-index change in quantum-well lasers," *IEEE Journal of Selected Topics in Quantum Electronics*, vol. 5, no. 3, pp. 637–642, 1999.

[74] E. Gehrig and O. Hess, *Spatio-Temporal Dynamics and Quantum Fluctuations in Semiconductor Lasers*. Springer, Nov. 2003.

[75] M. Radziunas, V. Z. Tronciu, U. Bandelow, M. Lichtner, M. Spreemann, and H. Wenzel, "Mode transitions in distributed-feedback tapered master-oscillator power-amplifier: theory and experiments," *Optical and Quantum Electronics*, vol. 40, pp. 1103–1109, Nov. 2008.

[76] O. Qasaimeh, "Dynamics of optical pulse amplification and saturation in multiple state quantum dot semiconductor optical amplifiers," *Optical and Quantum Electronics*, vol. 41, pp. 99–111, Jan. 2009.

[77] J. Cartledge and R. Srinivasan, "Extraction of DFB laser rate equation parameters for system simulation purposes," *Journal of Lightwave Technology*, vol. 15, pp. 852–860, May 1997.

[78] M. J. Adams, "Rate equations and transient phenomena in semiconductor lasers," *Opto-electronics*, vol. 5, pp. 201–215, Mar. 1973.

[79] P. Downey, J. Bowers, R. Tucker, and E. Agyekum, "Picosecond dynamics of a gain-switched InGaAsP laser," *IEEE Journal of Quantum Electronics*, vol. 23, no. 6, pp. 1039–1047, 1987.

[80] G. P. Agrawal and N. K. Dutta, "Rate Equations and Operating Characteristics," in *Semiconductor Lasers*, pp. 231–318, Springer US, Jan. 1993.

[81] S. A. Javro and S.-M. Kang, "Transforming Tucker's linearization laser rate equations to a form that has a single solution regime," *Journal of Lightwave Technology*, vol. 13, no. 9, pp. 1899–1904, 1995.

[82] P. M. Student, P. V. Mena, S. Member, S.-m. s. Kang, T. A. Detemple, and S. Member, "Rate-Equation-Based Laser Models with a Single Solution Regime," *Journal of lightwave Technology*, vol. 15, 1997.

[83] G. Agrawal, "Effect of gain and index nonlinearities on single-mode dynamics in semiconductor lasers," *IEEE Journal of Quantum Electronics*, vol. 26, no. 11, pp. 1901–1909, 1990.

[84] S. Chen, M. Yoshita, T. Ito, T. Mochizuki, H. Akiyama, and H. Yokoyama, "Gain-switched pulses from InGaAs ridge-quantum-well lasers limited by intrinsic dynamical gain suppression," *Optics Express*, vol. 21, pp. 7570–7576, Mar. 2013.

[85] G. A. P. Thé, M. Gioannini, and I. Montrosset, "Numerical analysis of the effects of carrier dynamics on the switch-on and gain-switching of quantum dot lasers," *Optical and Quantum Electronics*, vol. 40, pp. 1111–1116, Nov. 2008.

[86] T. Sogawa and Y. Arakawa, "Picosecond spectral dynamics of gain-switched quantum-well lasers and its dependence on quantum-well structures," *Journal of Applied Physics*, vol. 67, pp. 2675–2677, Mar. 1990.

[87] T. Sogawa and Y. Arakawa, "Picosecond lasing dynamics of gain-switched quantum well lasers and its dependence on quantum well structures," *IEEE Journal of Quantum Electronics*, vol. 27, no. 6, pp. 1648–1654, 1991.

[88] S. Riecke, *Flexible Generation of Picosecond Laser Pulses in the Infrared and Green Spectral Range by Gain-Switching of Semiconductor Lasers*, vol. 15 of *Innovationen mit Mikrowellen und Licht. Forschungsberichte aus dem Ferdinand-Braun-Institut, Leibniz-Institut für Höchstfrequenztechnik*. Göttingen: Culliver, 1 ed., Mar. 2011.

[89] J. N. Walpole, "Semiconductor amplifiers and lasers with tapered gain regions," *Optical and Quantum Electronics*, vol. 28, pp. 623–645, June 1996.

[90] EagleYard, "Data Sheet EYP-TPA-0780-02000-4006-CMT04-0000-105, http://www.eagleyard.com," 2009. Data sheet.

[91] G. Bendelli, K. Komori, S. Arai, and Y. Suematsu, "A new structure for high-power TW-SLA (Travelling wave semiconductor laser amplifier)," *IEEE Photonics Technology Letters*, vol. 3, pp. 42–44, Jan. 1991.

[92] J. N. Walpole, E. S. Kintzer, S. R. Chinn, C. A. Wang, and L. J. Missaggia, "High-power strained-layer InGaAs/AlGaAs tapered traveling wave amplifier," *Applied Physics Letters*, vol. 61, pp. 740–742, Aug. 1992.

[93] D. Mehuys, D. Welch, and L. Goldberg, "2.0 W CW, diffraction-limited tapered amplifier with diode injection," *Electronics Letters*, vol. 28, pp. 1944–1946, Oct. 1992.

[94] E. Kintzer, J. Walpole, S. Chinn, C. Wang, and L. Missaggia, "High-power, strained-layer amplifiers and lasers with tapered gain regions," *IEEE Photonics Technology Letters*, vol. 5, pp. 605 –608, June 1993.

[95] V. Bolpasi and W. von Klitzing, "Double-pass tapered amplifier diode laser with an output power of 1 W for an injection power of only $200 \mu W$," *Review of Scientific Instruments*, vol. 81, pp. 113108–113108–4, Nov. 2010.

[96] N. K. Dutta and Q. Wang, *Semiconductor optical amplifiers*. World Scientific Publishing Company, 2 ed., 2013.

[97] H. Ghafouri-Shiraz, P. W. Tan, and T. Aruga, "Picosecond pulse amplification in tapered-waveguide laser-diode amplifiers," *IEEE Journal of Selected Topics in Quantum Electronics*, vol. 3, no. 2, pp. 210–217, 1997.

[98] P. W. Tan and H. Ghafouri-Shiraz, "Sub-picosecond gain dynamic in highly index-guided tapered-waveguide laser diode optical amplifiers," *Optoelectronics, IEE Proceedings* -, vol. 146, no. 2, pp. 83–88, 1999.

[99] E. Gehrig and O. Hess, "Optimization of tapered semiconductor optical amplifiers for picosecond pulse amplification," *Applied Physics Letters*, vol. 87, p. 251106, Dec. 2005.

[100] C. Pfahler, M. Eichhorn, M. T. Kelemen, G. Kaufel, M. Mikulla, J. Schmitz, and J. Wagner, "Gain saturation and high-power pulsed operation of GaSb-based tapered diode lasers with separately contacted ridge and tapered section," *Applied Physics Letters*, vol. 89, pp. 021107–021107–3, July 2006.

[101] S. Riecke, S. Schwertfeger, K. Lauritsen, K. Paschke, R. Erdmann, and G. Tränkle, "23W peak power picosecond pulses from a single-stage all-semiconductor master oscillator power amplifier," *Applied Physics B: Lasers and Optics*, vol. 98, no. 2, pp. 295–299, 2010.

[102] S. M. Riecke, K. Lauritsen, R. Erdmann, M. Uebernickel, K. Paschke, and G. Erbert, "Pulse-shape improvement during amplification and second-harmonic generation of picosecond pulses at 531?nm," *Optics Letters*, vol. 35, pp. 1500–1502, May 2010.

[103] A. Klehr, A. Liero, T. Hoffmann, S. Schwertfeger, H. Wenzel, G. Erbert, W. Heinrich, and G. Tränkle, "Compact ps-pulse laser source with free adjustable repetition rate and nJ pulse energy on microbench," *SPIE Proceedings*, vol. 7953, pp. 79531D–79531D, Feb. 2011.

[104] S. Schwertfeger, A. Klehr, T. Hoffmann, A. Liero, H. Wenzel, and G. Erbert, "Generation of sub-100 ps pulses with a peak power of 65 W by gain switching, pulse shortening, and pulse amplification using a semiconductor-based master oscillator–power amplifier system," *Applied Optics*, vol. 52, pp. 3364–3367, May 2013.

[105] A. Liero, A. Klehr, S. Schwertfeger, T. Hoffmann, and W. Heinrich, "Laser driver switching 20 A with 2 ns pulse width using GaN," in *Microwave Symposium Digest (MTT), 2010 IEEE MTT-S International*, pp. 1110 –1113, May 2010.

[106] E. Mohadesrad and K. Abedi, "Proposal for modeling of tapered quantum-dot semiconductor optical amplifiers," *Frontiers of Optoelectronics*, vol. 5, pp. 457–464, Dec. 2012.

[107] C. Mesaritakis, A. Kapsalis, H. Simos, C. Simos, M. Krakowski, I. Krestnikov, and D. Syvridis, "Tapered InAs/InGaAs quantum dot semiconductor optical amplifier design for enhanced gain and beam quality," *Optics Letters*, vol. 38, pp. 2404–2406, July 2013.

[108] X. Wang, G. Erbert, H. Wenzel, B. Eppich, P. Crump, A. Ginolas, J. Fricke, F. Bugge, M. Spreemann, and G. Tränkle, "High-power, spectrally stabilized, near-diffraction-limited 970 nm laser light source based on truncated-tapered semiconductor optical amplifiers with low confinement factors," *Semiconductor Science and Technology*, vol. 27, p. 015010, Jan. 2012.

[109] X. Wang, G. Erbert, H. Wenzel, P. Crump, B. Eppich, S. Knigge, P. Ressel, A. Ginolas, A. Maassdorf, and G. Trankle, "17-W Near-Diffraction-Limited

970-nm Output From a Tapered Semiconductor Optical Amplifier," *IEEE Photonics Technology Letters*, vol. 25, no. 2, pp. 115–118, 2013.

[110] H. Odriozola, J. M. G. Tijero, I. Esquivias, L. Borruel, A. Martín-Mínguez, N. Michel, M. Calligaro, M. Lecomte, O. Parillaud, M. Ruiz, and M. Krakowski, "Design of 1060nm tapered lasers with separate contacts," *Optical and Quantum Electronics*, vol. 40, pp. 1123–1127, Nov. 2008.

[111] V. Z. Tronciu, M. Lichtner, M. Radziunas, U. Bandelow, and H. Wenzel, "Improving the stability of distributed-feedback tapered master-oscillator power-amplifiers," *Optical and Quantum Electronics*, vol. 41, pp. 531–537, May 2009.

[112] C. Fiebig, V. Z. Tronciu, M. Lichtner, K. Paschke, and H. Wenzel, "Experimental and numerical study of Distributed-Bragg-Reflector tapered lasers," *Applied Physics B*, vol. 99, pp. 209–214, Apr. 2010.

[113] D. Feise, W. John, F. Bugge, C. Fiebig, G. Blume, and K. Paschke, "High-spectral-radiance, red-emitting tapered diode lasers with monolithically integrated distributed Bragg reflector surface gratings," *Optics Express*, vol. 20, pp. 23374–23382, Oct. 2012.

[114] F. Kappeler, K. Mettler, and K.-H. Zschauer, "Pulsed-power performance and stability of 880 nm GaAlAs/GaAs oxide-stripe lasers," *Solid-State and Electron Devices, IEE Proceedings I*, vol. 129, pp. 256–261, Dec. 1982.

[115] M. Ziegler, M. Hempel, H. E. Larsen, J. W. Tomm, P. E. Andersen, S. Clausen, S. N. Elliott, and T. Elsaesser, "Physical limits of semiconductor laser operation: A time-resolved analysis of catastrophic optical damage," *Applied Physics Letters*, vol. 97, p. 021110, July 2010.

[116] M. B. Danailov and P. Apai, "589 nm light generation by intracavity mixing in a Nd:YAG laser," *Journal of Applied Physics*, vol. 75, pp. 8240–8242, June 1994.

[117] T. Y. Fan and R. Byer, "Diode laser-pumped solid-state lasers," *IEEE Journal of Quantum Electronics*, vol. 24, pp. 895–912, June 1988.

[118] P. Cerny, H. Jelinkova, P. G. Zverev, and T. T. Basiev, "Solid state lasers with Raman frequency conversion," *Progress in Quantum Electronics*, vol. 28, no. 2, pp. 113–143, 2004.

[119] A. Liu, M. A. Norsen, and R. D. Mead, "60-W green output by frequency doubling of a polarized Yb-doped fiberlaser," *Optics Letters*, vol. 30, pp. 67–69, Jan. 2005.

[120] D. Skoczowsky, A. Jechow, R. Menzel, K. Paschke, and G. Erbert, "Efficient second-harmonic generation using a semiconductor tapered amplifier in a coupled ring-resonator geometry," *Optics Letters*, vol. 35, pp. 232–234, Jan. 2010.

[121] J. Webjorn, F. Laurell, and G. Arvidsson, "Blue light generated by frequency doubling of laser diode light in a lithium niobate channel waveguide," *IEEE Photonics Technology Letters*, vol. 1, pp. 316–318, Oct. 1989.

[122] M. Rusu, E. U. Rafailov, R. Herda, O. G. Okhotnikov, S. M. Saltiel, P. Battle, S. McNeil, A. B. Grudinin, and W. Sibbett, "Efficient generation of green and UV light in a single PP-KTP waveguide pumped by a compact all-fiber system," *Applied Physics Letters*, vol. 88, p. 121105, Mar. 2006.

[123] K. A. Fedorova, G. S. Sokolovskii, D. I. Nikitichev, P. R. Battle, I. L. Krestnikov, D. A. Livshits, and E. U. Rafailov, "Orange-to-red tunable picosecond pulses by frequency doubling in a diode-pumped PPKTP waveguide," *Optics Letters*, vol. 38, pp. 2835–2837, Aug. 2013.

[124] K. Y. Han, K. I. Willig, E. Rittweger, F. Jelezko, C. Eggeling, and S. W. Hell, "Three-Dimensional Stimulated Emission Depletion Microscopy of Nitrogen-Vacancy Centers in Diamond Using Continuous-Wave Light," *Nano Letters*, vol. 9, pp. 3323–3329, Sept. 2009.

[125] E. Rittweger, K. Y. Han, S. E. Irvine, C. Eggeling, and S. W. Hell, "STED microscopy reveals crystal colour centres with nanometric resolution," *Nature Photonics*, vol. 3, pp. 144–147, Mar. 2009.

[126] S. Arroyo-Camejo, M.-P. Adam, M. Besbes, J.-P. Hugonin, V. Jacques, J.-J. Greffet, J.-F. Roch, S. W. Hell, and F. Treussart, "Stimulated Emission Depletion Microscopy Resolves Individual Nitrogen Vacancy Centers in Diamond Nanocrystals," *ACS Nano*, Nov. 2013.

[127] D. L. Staebler and S. E. Schnatterly, "Optical Studies of a Photochromic Color Center in Rare-Earth-Doped CaF2," *Physical Review B*, vol. 3, pp. 516–526, Jan. 1971.

[128] J. M. Flaherty, "A Review of Depreciative Color Center Phenomena in Lamp Phosphors," *Journal of The Electrochemical Society*, vol. 128, pp. 131–139, Jan. 1981.

[129] A. V. Amossov and A. O. Rybaltovsky, "Radiation color center formation in silica glasses: a review of photo- and thermo-chemical aspects of the

problem," *Journal of Non-Crystalline Solids*, vol. 179, pp. 226–234, Nov. 1994.

[130] M. S. Akselrod, A. E. Akselrod, S. S. Orlov, S. Sanyal, and T. H. Underwood, "Fluorescent Aluminum Oxide Crystals for Volumetric Optical Data Storage and Imaging Applications," *Journal of Fluorescence*, vol. 13, pp. 503–511, Nov. 2003.

[131] G. M. Akselrod, M. S. Akselrod, E. R. Benton, and N. Yasuda, "A novel Al2O3 fluorescent nuclear track detector for heavy charged particles and neutrons," *Nuclear Instruments and Methods in Physics Research Section B: Beam Interactions with Materials and Atoms*, vol. 247, pp. 295–306, June 2006.

[132] M. Niklas, A. Abdollahi, M. S. Akselrod, J. Debus, O. Jäkel, and S. Greilich, "Subcellular Spatial Correlation of Particle Traversal and Biological Response in Clinical Ion Beams," *International Journal of Radiation Oncology*Biology*Physics*, vol. 87, pp. 1141–1147, Dec. 2013.

[133] M. Niklas, J. A. Bartz, M. S. Akselrod, A. Abollahi, O. Jäkel, and S. Greilich, "Ion track reconstruction in 3D using alumina-based fluorescent nuclear track detectors," *Physics in Medicine and Biology*, vol. 58, p. N251, Sept. 2013.

[134] M. Niklas, C. Melzig, A. Abdollahi, J. Bartz, M. S. Akselrod, J. Debus, O. Jäkel, and S. Greilich, "Spatial correlation between traversal and cellular response in ion radiotherapy – Towards single track spectroscopy," *Radiation Measurements*, vol. 56, pp. 285–289, Sept. 2013.

[135] F. W. Grover, *Inductance calculations: working formulas and tables*. Mineola, N.Y.: Dover Publications, 2004.

[136] K. Kolmakov, C. A. Wurm, R. Hennig, E. Rapp, S. Jakobs, V. N. Belov, and S. W. Hell, "Red-Emitting Rhodamines with Hydroxylated, Sulfonated, and Phosphorylated Dye Residues and Their Use in Fluorescence Nanoscopy," *Chemistry – A European Journal*, vol. 18, no. 41, p. 12986–12998, 2012.

[137] M. V. Sednev, C. A. Wurm, V. N. Belov, and S. W. Hell, "Carborhodol: A New Hybrid Fluorophore Obtained by Combination of Fluorescein and Carbopyronine Dye Cores," *Bioconjugate Chemistry*, vol. 24, pp. 690–700, Apr. 2013.

[138] K. Kolmakov, C. A. Wurm, D. N. H. Meineke, F. Göttfert, V. P. Boyarskiy, V. N. Belov, and S. W. Hell, "Polar Red-Emitting Rhodamine Dyes with Reactive Groups: Synthesis, Photophysical Properties, and Two-Color STED

Nanoscopy Applications," *Chemistry – A European Journal*, vol. 20, no. 1, p. 146–157, 2014.

[139] EagleYard, "Data Sheet EYP-RWL-0808-00800-4000-BFW02-0010.pdf, http://www.eagleyard.com," 2012. Data sheet.

[140] Oclaro, "Data Sheet HL6545MG_Rev7," 2013. Data sheet.

[141] F. Görlitz, "Aufbau eines mehrkanaligen STED Mikroskops für Biomedizinische Anwendungen," 2013. Master Thesis.

[142] A. C. Wilson, J. C. Sharpe, C. R. McKenzie, P. J. Manson, and D. M. Warrington, "Narrow-Linewidth Master-Oscillator Power Amplifier Based on a Semiconductor Tapered Amplifier," *Applied Optics*, vol. 37, pp. 4871–4875, July 1998.

[143] M. Chi, O. B. Jensen, J. Holm, C. Pedersen, P. E. Andersen, G. Erbert, B. Sumpf, and P. M. Petersen, "Tunable high-power narrow-linewidth semiconductor laser based on an external-cavity tapered amplifier," *Optics Express*, vol. 13, pp. 10589–10596, Dec. 2005.

[144] T. N. Vu, A. Klehr, B. Sumpf, H. Wenzel, G. Erbert, and G. Tränkle, "Wavelength stabilized ns-MOPA diode laser system with 16 W peak power and a spectral line width below 10 pm," *Semiconductor Science and Technology*, vol. 29, p. 035012, Mar. 2014.

Acknowledgements

During my work which led to this thesis I have enjoyed the support from a whole number of people. Despite at the last position of this document, they were by no means least important for the success of my work. For this, I would like to express my gratitude:
To Professor Stefan W. Hell for giving me the possibility to work on this topic. I have enjoyed to work under his supervision and to have had the opportunity to share his views on physics, whether connected to his field or not.
To Professor Wolfgang Petrich for agreeing to be second referee.
To Professor Wolfhard Semmler for being member of my TAC.
To Johann Engelhardt for the tremendous support he could provide for literally any issue I managed to come up with. I am very glad I had the opportunity to learn from him.
To all my colleagues in the Heidelberg Hell group for creating an atmosphere in which it was so much fun to work. In particular this is my office crew, thanks for the fruitful discussions to Lucas Alber, Fabian Bergermann, Pit Bingen, Nikolas Dimitriadis, Frederik Görlitz and Patrick Hoyer. Many thanks to the girls' office, in particular Franziska Curdt, Dörte Oltmanns, Jale Schneider and Jasmin Zahn, for criminally organized Kuchen, fondue and birthday presents.
For careful proofreading I want to thank Fabian Bergermann, Patrick Hoyer, Rahul Nair and Johann Engelhardt.
I would like to thank the DKFZ machine shop, in particular Heinrich Rühle and Wolfram Stroh, for most accurately fabricated parts of whatever shape.
Thanks to Martin Niklas for the cool application for TA STED he came up with.

Außerdem gibt es ein Leben neben der Arbeit, ohne das meine Arbeit so nicht möglich gewesen wäre. Deshalb geht mein großer Dank an diejenigen, die mich begleitet haben.
An Marieke dafür, dass du "stets meine engste Weggefährtin" bist.
An meine Mutter für bedingunslosen Rückhalt, an Michael und Manuel dafür, dass sie ebenfalls immer für mich da sind.
Außerdem Alonja, Bene, Evi, Doro, Hans, Jan, Jana, Jay, Linda, Maxim, Löffel, Matthias, Niki, Pierre, Rahul, Robin, Steffi, Timo, Wiwi.